



ESA CONTRACT REPORT

Contract Report to the European Space Agency

Tech Note - Phase II - WP1100
SMOS Monitoring Report
Number 4: Jan 2013 - Dec 2013

Joaquín Muñoz Sabater,
Mohamed Dahoui,
Patricia de Rosnay,
Lars Isaksen

ESA/ESRIN Contract
4000101703/10/NL/FF/fk

European Centre for Medium-Range Weather Forecasts
Europäisches Zentrum für mittelfristige Wettervorhersage
Centre européen pour les prévisions météorologiques à moyen terme

Series: ECMWF ESA Project Report Series

A full list of ECMWF Publications can be found on our web site under:

<http://www.ecmwf.int/publications/>

Contact: library@ecmwf.int

©Copyright 2014

European Centre for Medium Range Weather Forecasts
Shinfield Park, Reading, RG2 9AX, England

Literary and scientific copyrights belong to ECMWF and are reserved in all countries. This publication is not to be reprinted or translated in whole or in part without the written permission of the Director-General. Appropriate non-commercial use will normally be granted under the condition that reference is made to ECMWF.

The information within this publication is given in good faith and considered to be true, but ECMWF accepts no liability for error, omission and for loss or damage arising from its use.

Tech Note - Phase II - WP1100
SMOS Monitoring Report
Number 4: Jan 2013 - Dec 2013

*Authors: Joaquín Muñoz Sabater,
Mohamed Dahoui,
Patricia de Rosnay,
Lars Isaksen*

Technical Note - Phase-II - WP1100
Monitoring Report Number 4: Jan 2013 - Dec 2013
ESA/ESRIN Contract 4000101703/10/NL/FF/fk

European Centre for Medium-Range Weather Forecasts
Shinfield Park, Reading, Berkshire, UK

Jan 2014

	Name	Company
First version prepared by (January 2014)	J. Muñoz Sabater	ECMWF
Quality Visa	E. Källén	ECMWF
Application Authorized by		ESA/ESTEC

Distribution list:

ESA/ESRIN

Luc Govaert
Susanne Mecklenburg
Steven Delwart
ESA ESRIN Documentation Desk

SERCO

Raffaele Crapolicchio

ESA/ESTEC

Tania Casal
Matthias Drusch
Klaus Scipal

ECMWF

HR
Division & Section Heads

Contents

1	Introduction	2
2	SMOS observations at ECMWF	3
3	Monitoring over land	3
3.1	Simulations of brightness temperatures	3
3.2	Time-averaged geographical mean fields.	4
3.3	Time series	13
3.4	Angular distribution of bias	22
3.5	Hovmöller plots	25
4	Monitoring over oceans	29
4.1	Time-averaged geographical mean fields.	29
4.2	Hovmöller plots	34
5	Summary	36
6	References	38

Abstract

Contracted by the European Space Agency (ESA), the European Centre for Medium-Range Weather Forecasts (ECMWF) is involved in global monitoring and data assimilation of the Soil Moisture and Ocean Salinity (SMOS) mission data. For the first time, a new innovative remote sensing technique based on radiometric aperture synthesis is used in SMOS to observe soil moisture over continental surfaces and ocean salinity over oceans. Monitoring SMOS data (i.e. the comparison between the observed value and the model equivalent of that observation) is therefore of special interest and a requirement prior to assimilation experiments. This report is the fourth Monitoring Report delivered to ESA. The objective is to report on the monitoring activities of SMOS data over land and sea on a long term basis, investigating also the multi-angular and multi-polarised aspect of the SMOS observations. This report presents SMOS data monitoring results for the whole year 2013, using Near Real Time (NRT) data. It is worth mentioning that the SMOS monitoring research suite was substituted by the operational suite in July 2013, within ECMWF cycle 38r2, as it will be observed in some plots of this report.

1 Introduction

ECMWF has developed an operational chain which monitors SMOS data in Near Real Time (NRT) at global scale, as explained in (Muñoz-Sabater et al. 2010). Monitoring is carried out routinely for each new type of satellite data brought into the operational Integrated Forecasting System (IFS) at ECMWF. In Numerical Weather Prediction systems monitoring is mainly focused on the comparison between the observed variable and the model equivalent simulating that observation, because this is the quantity used in the analysis.

For SMOS, monitoring is produced separately for land and oceans. The reason is the strong contrast between the dielectric constant of water bodies and land surfaces, which in turn produces very different emissivities and observed brightness temperatures at the top of the atmosphere. Thus, monitoring SMOS data separately over land and oceans increases the sensitivity to the statistical variables. Moreover, the multi-angular and multi-polarised aspect of the observations is also accounted for in the monitoring chain by monitoring the data independently for several incidence angles of the observations and for two polarisation states at the antenna reference frame.

The developed framework makes it possible to obtain daily statistics of the observations, the model equivalent of the observations computed by the Community Microwave Emission Modelling (CMEM) platform (Drusch et al. 2009; de Rosnay et al. 2009a), and the difference between the two quantities, the so called first-guess departures. The statistics are computed over several weeks of data. This is a very robust way to identify systematic differences between modelled values and observations. Furthermore it also set the basis to investigate and understand the new observations before they become active in the ECMWF land assimilation scheme.

This Monitoring Report (MR4) on SMOS data is the fourth monitoring report delivered to ESA. In the first one (Muñoz-Sabater et al. 2011b) the monitoring website and statistical products were described. The second one (Muñoz-Sabater et al. 2011a) showed results obtained in NRT for the period November 2010- November 2011, whereas in the third one (Muñoz-Sabater et al. 2013a) the period studied was December 2011- December 2012. This document monitors the whole year 2013 and it follows the same structure as the previous report.

2 SMOS observations at ECMWF

SMOS NRT products are processed at the European Space Astronomy Centre (ESAC) in Madrid (Spain) and sent to ECMWF via the SMOS Data Processing Ground Segment (DPGS) interface. The product used at ECMWF is the NRT product which are geographically sorted swath-based maps of brightness temperatures. The geolocated product received at ECMWF is arranged in an equal area grid system called ISEA 4H9 (Icosahedron Snyder Equal Area grid with Aperture 4 at resolution 9) [see (Matos and Gutierrez 2004)]. For this grid, the centre of the cell grids are at equal distance of 15 km over land, with a standard deviation of 0.9 km. For the NRT product, the resolution is coarser over oceans as they present lower heterogeneities than continental surfaces. The format of the NRT product is the Binary Universal Form for the Representation of meteorological data (BUFR). Each message in BUFR format corresponds to a snapshot where the integration time is 1.2 seconds. On average, each snapshot contains around 4800 subsets over land.

3 Monitoring over land

In this section some of the most relevant results over land surfaces, partly obtained with the monitoring suite developed for SMOS [see a description in part III of (Muñoz-Sabater et al. 2010) and (Muñoz-Sabater et al. 2011b)] and partly with the operational suite, are shown.

3.1 Simulations of brightness temperatures

In order to simulate brightness temperatures at L-band and compare them to the SMOS observations, ECMWF developed the Community Microwave Emission Modelling (CMEM) platform (de Rosnay et al. 2009b). It constitutes the forward model operator for low frequency passive microwave brightness temperatures of the surface. Although for SMOS purposes it is used at 1.4 GHz, potentially it can be used up to 20 GHz. This software package is fully coded in Fortran-90 language. It has been designed to be highly modular providing a good range of I/O interfaces for the Numerical Weather Prediction Community. CMEM surface forcing comes from the integration of the operational H-TESSSEL (Hydrology Tiled ECMWF Scheme for Surface Exchanges over Land) land surface scheme (Balsamo et al. 2009). H-TESSSEL is forced with meteorological fields of surface pressure, specific humidity, air temperature and wind speed at the lowest atmospheric level. The surface radiation and precipitation flux represent 3 hourly averages, and they are kept constant over a 3 hour period. The integration of H-TESSSEL provides the soil moisture and soil temperature fields, as well as snow depth and snow density fields, which are then coupled with CMEM to simulate ECMWF first-guess L-band brightness temperatures. Additional land surface information needed is soil texture data obtained from the Food and Agriculture Organization (FAO) data set, whereas sand and clay fractions have been computed from a lookup table according to (Salgado 1999). The soil roughness standard deviation of height (σ) parameter in CMEM is set to 2.2 cm as in (Holmes et al. 2008). Vegetation type is derived from the H-TESSSEL classification, whereas a MODIS climatology is used to derive leaf area index (LAI).

CMEM's physics is based on the parameterisations used in the L-Band Microwave Emission of the Biosphere [LMEB, (Wigneron et al. 2007)] and Land Surface Microwave Emission Model [LSMEM, (Drusch et al. 2001)]. The modular architecture of CMEM makes it possible to consider different parameterisations of the soil dielectric constant, the effective temperature, the roughness effect of the soil and the vegetation and atmospheric contribution opacity models. In the offline SMOS monitoring suite until July 2013, the vegetation opacity model of (Kirdyashev et al. 1979) was used in combination with (Wang and Schmugge 1980) dielectric model, (Wigneron et al. 2001) effective temperature model, the simple soil roughness model of (Choudhury et al. 1979)

and the atmospheric contribution of (Pellarin et al. 2003).

This combination of parameterisations were shown to be well suited for brightness temperature modelling (Drusch et al. 2009; de Rosnay et al. 2009a; Muñoz-Sabater et al. 2011c). However these results were based on local and regional scale experiments. A global sensitivity study with SMOS data was conducted in early 2013 for assimilation purposes. At the time that the CMEM platform was implemented operationally, the preliminary global calibration study indicated that the most suited combination of CMEM parameterisations for assimilation purposes was; (Mironov et al. 2004) for the dielectric model, (Wigneron et al. 2001) for the soil roughness and (Jackson and Schmugge 1991) for the vegetation opacity model. These set of parameterisations produced simulated brightness temperatures closer to the reprocessed SMOS NRT product, and since 25 July 2013 (within the operational ECMWF cycle 38r2) they substituted the previous set of parameterisations in the SMOS monitoring suite. However, the previous global calibration study was not complete and new changes were introduced in ECMWF cycle cy40r1, which accounted for the most calibrated CMEM platform, as reported in (de Rosnay et al. 2014). The parameterisations which were changed are (Wang and Schmugge 1980) for the dielectric model and (Wigneron et al. 2007) for the vegetation emissivity. These changes entered into operations on 19 November 2013 and no further changes are expected in the next cycles.

3.2 Time-averaged geographical mean fields.

Fig. 1 and Fig. 2 show the observed brightness temperatures, for August 2013, as a function of six incidence angles multiples of 10, averaged in boxes of 0.25 degrees. Fig. 1 is for XX polarisation whereas Fig. 2 is for YY polarisation. They show monthly averages for August 2013, using the operational cycle cy38r2. Observations out of the [50,350] K interval were rejected as not being considered physically realistic. To eliminate the influence of snow or frozen soils, these grid points were previously filtered out too, based on snow depth and 2 m temperature forecast fields. Both polarisations behave as theoretically expected at global scale, i.e., brightness temperatures decreasing with the incidence angle for XX polarisation (from a global mean average of 255.5 at 10 degrees to 235.3 at 60 degrees) and increasing for YY polarisation (from 256.5 at 10 degrees to 273.1 at 60 degrees).

Fig. 3 shows the evolution of the SMOS observed brightness temperatures standard deviation at global scale, from January to October 2013 (one averaged value per month), at 40 degrees incidence angle and for XX polarisation. Fig. 4 is the equivalent figure for YY polarisation. These statistics are also computed in spatial boxes of 0.25 degrees. Most of the largest values of the observations variability, in dark red colour (especially in Europe and Asia), are due to Radio Frequency Interference (RFI). They not only point to RFI sources, but also to areas contaminated by them, which can reach hundred of km away from the source. The sources of RFI in China, Western Europe and Eurasia are clear in these plots. However it can be observed that from May 2013 the area strongly affected by RFI decreases gradually, and by October 2013 the contamination is much lower than at the beginning of the year. This is more clear in XX polarisation than in YY polarisation, as the latter is, in general, more sensitive to RFI. It can also be observed, from June 2013, the appearance of a new source in Northwest of Africa, affecting more XX polarisation than YY polarisation. In general, all America, South of Africa and Australia are clean of RFI, and over there larger standard deviation (STD) of the observations can be associated to areas reflecting a good natural monthly range of brightness temperatures. These areas are very important for assimilation experiments. Also, the most western part of Europe is relatively clean, which depicts a complete different picture compared to the first year of the SMOS mission. It is also worth mentioning that although the area affected by RFI is smaller by the end of the year than at the beginning of the year, the mean global average of the observations STD is larger for the former. This may seem contradictory, however the number of grid points used to average the data is different from the period January-July 2013 than from August onwards, when SMOS monitoring entered into operations and snow and frozen soils were filtered out. For example it

can be seen that from August 2013, statistics are not produced over the poles, as they were completely covered by ice and snow. Before August 2013 a compensating effect produced smaller global averaged values of the observations STD.

Figs. 5 and 6 show the evolution of the first-guess departures (observed brightness temperatures minus the model equivalents) at the antenna reference frame from January to October 2013 (one averaged value per month), at 40 degrees incidence angle and for XX and YY polarisations, respectively. As it occurred for the year 2012, the model clearly underestimates the observations over snow covered areas, while at global scale observed brightness temperatures are overestimated. At global scale, the snow effect compensates for the negative bias in XX polarisation, and this is the reason why, for those months showing the largest spatial coverage of snow, the mean bias are close to zero. From August 2013 (when SMOS monitoring entered in to operations), snow is filtered out from these statistics, and a more accurate roughness model significantly decreased the mean global bias, from -7.5 K to -2.6 K. From this month, it can be observed how the Arctic region is no longer accounted for in these statistics, and in October the northern latitudes of Asia are also filtered out. This is also another way to monitor the line of snow in the Northern Hemisphere. The sensitivity to snow and ice in the YY polarisation is much weaker, and as it happened for previous years, the mean bias are negative for all months, larger than -10 K. However, a decrease of 4.1 K is produced from July to August 2013. The sign of the bias is mixed at global scale for both polarisations, being the North of Canada, desert areas of Africa, Middle East and the West of Australia, the regions where observed brightness temperatures experience a larger overestimation. It is also important to mention that the bias showed in these figures are also angular dependent. This is discussed in section 3.4.

The particular situation of RFI in Europe is shown in Fig. 7, through first-guess departures in YY polarisation, because this polarisation is more sensitive to RFI. The punctual red dots observed in these plots show large disagreement between the observations and the model, and are linked to fixed sources of RFI. Although the situation is much improved compared to the same figure of year 2011 (see (Muñoz-Sabater et al. 2011a)), however no further improvement can be observed compared to 2012 (see same figure in (Muñoz-Sabater et al. 2013a)). Clear RFI sources are still present along 2013 in North Ireland, Madrid, London, Milan and Croatia. Their intensity is limited and the contaminated area seems to be mainly constrained to the location of the source. Apparently, the rest of Europe does not show strong contamination by RFI.

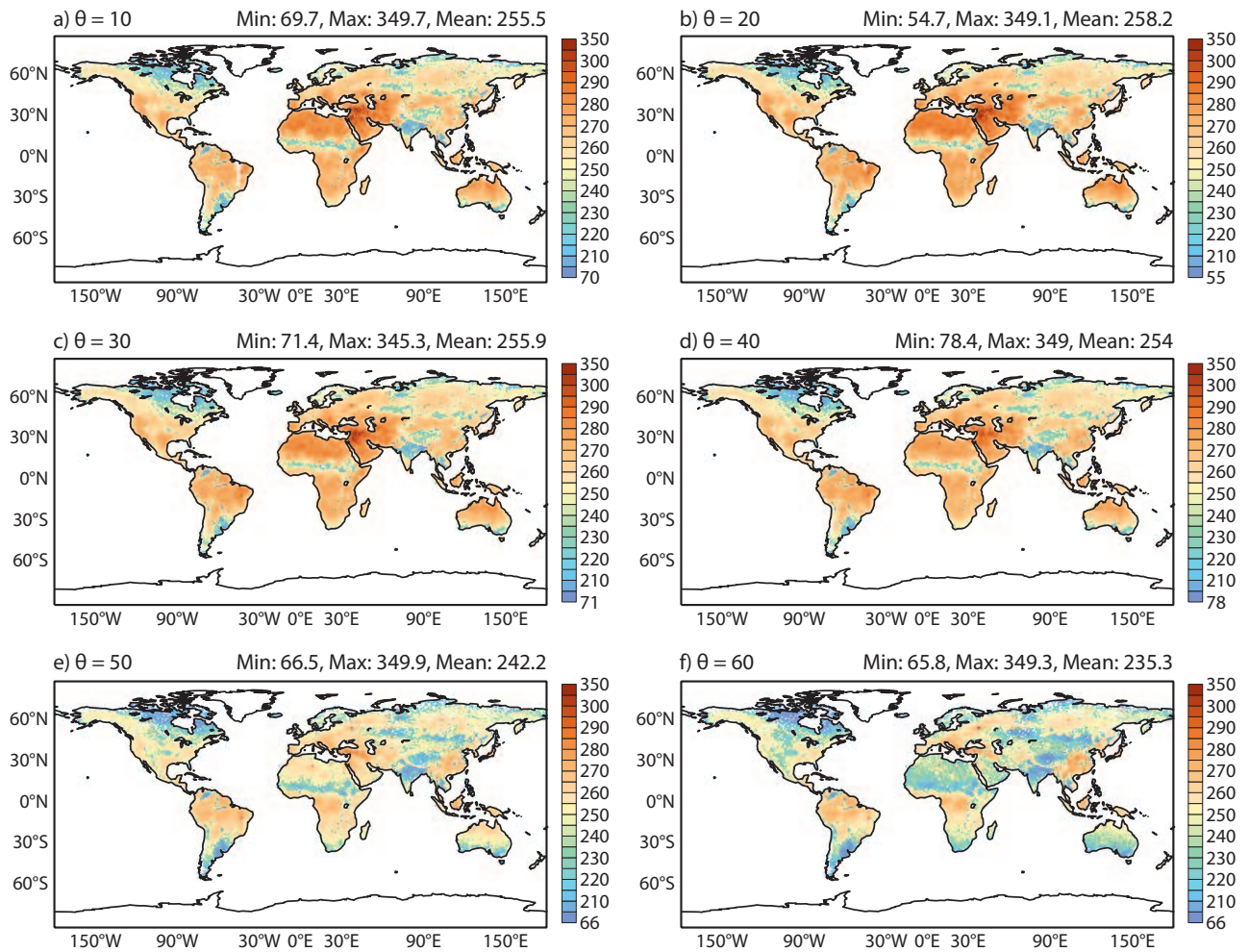


Figure 1: August 2013, geographical mean of the SMOS observed brightness temperatures as a function of the incidence angle, for XX polarisation. Each value represents a mean value of all the data inside a box of 0.25 degrees.

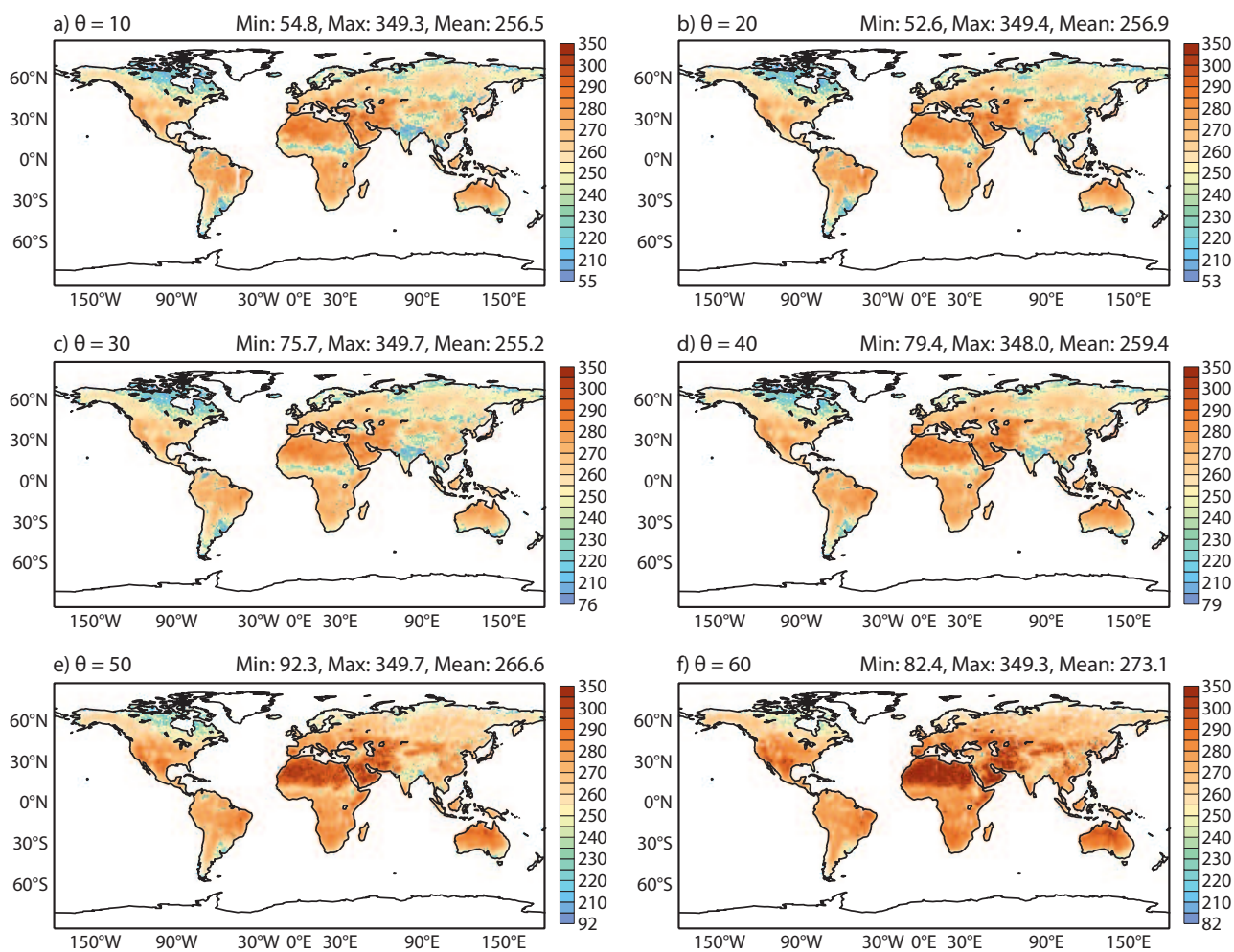


Figure 2: As in Fig. 1 but for YY polarisation.

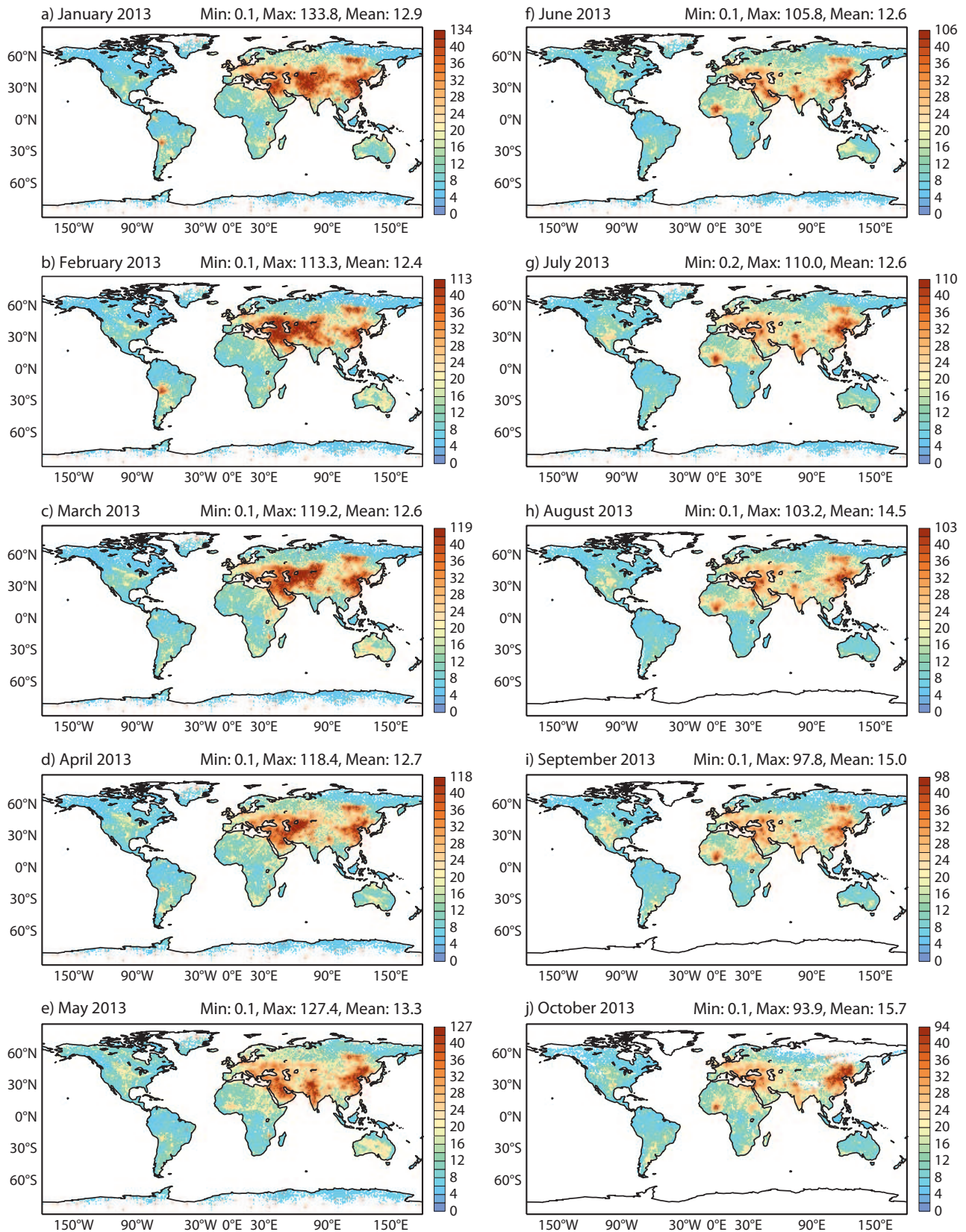


Figure 3: Monthly global mean of the SMOS observed brightness temperatures standard deviation, for XX polarisation, from January 2013 to October 2013. Each value represents a mean value of all the data inside a box of 0.25 degrees. The incidence angle is 40 degrees.

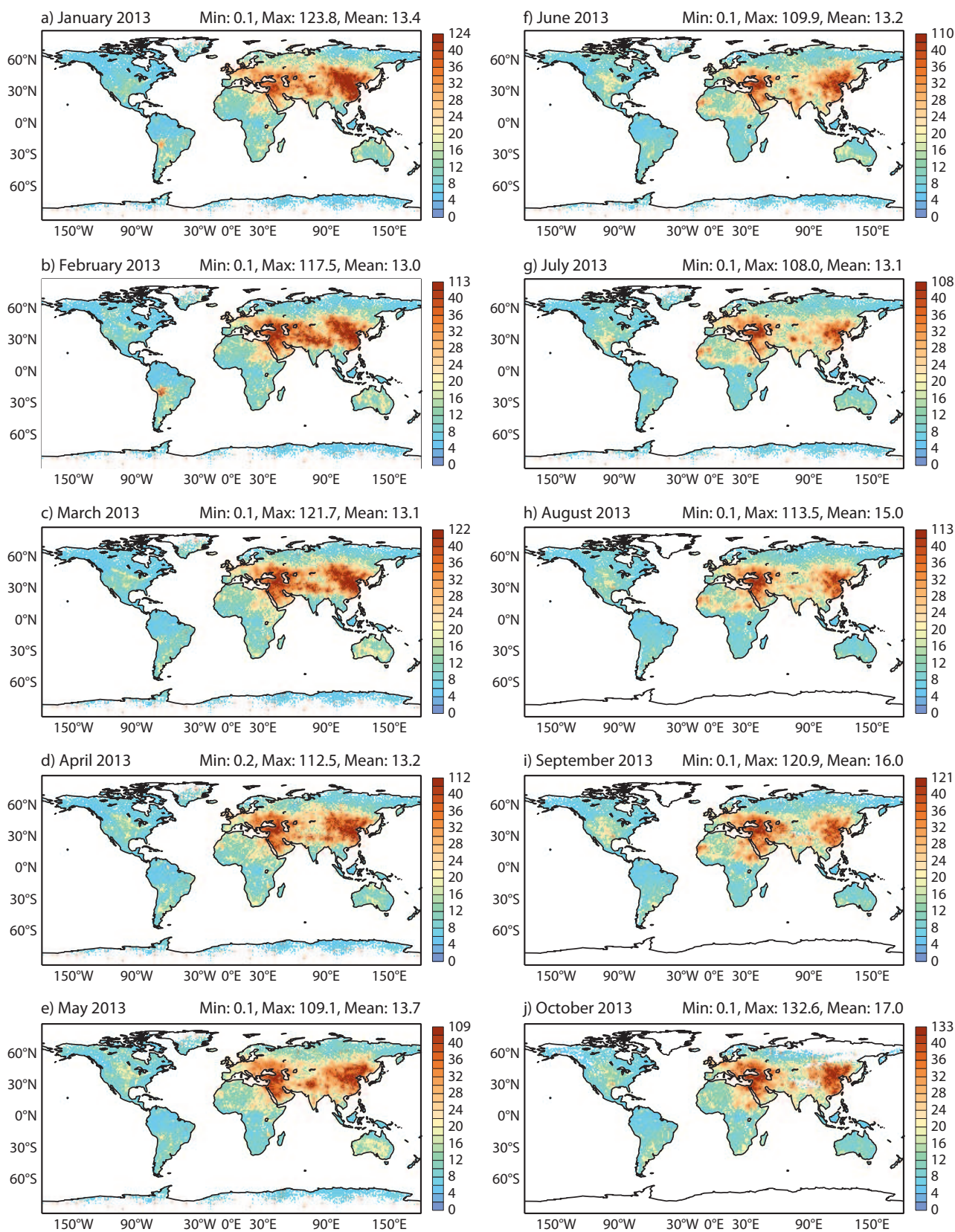


Figure 4: As Fig. 3, but for YY polarisation.

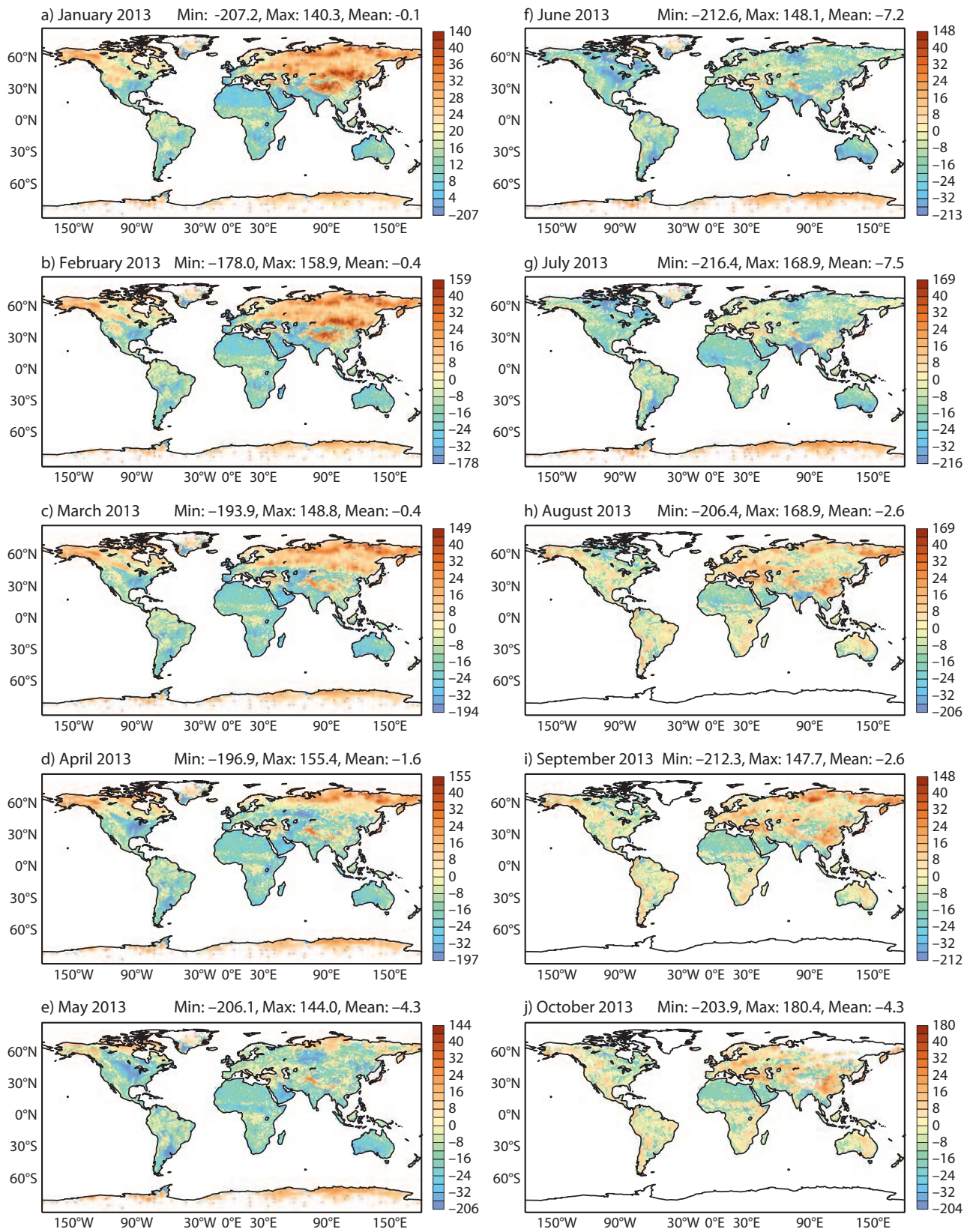


Figure 5: Monthly global mean of the first-guess departures between SMOS observed brightness temperatures and the CMEM equivalents, for XX polarisation at 40 degrees incidence angle.

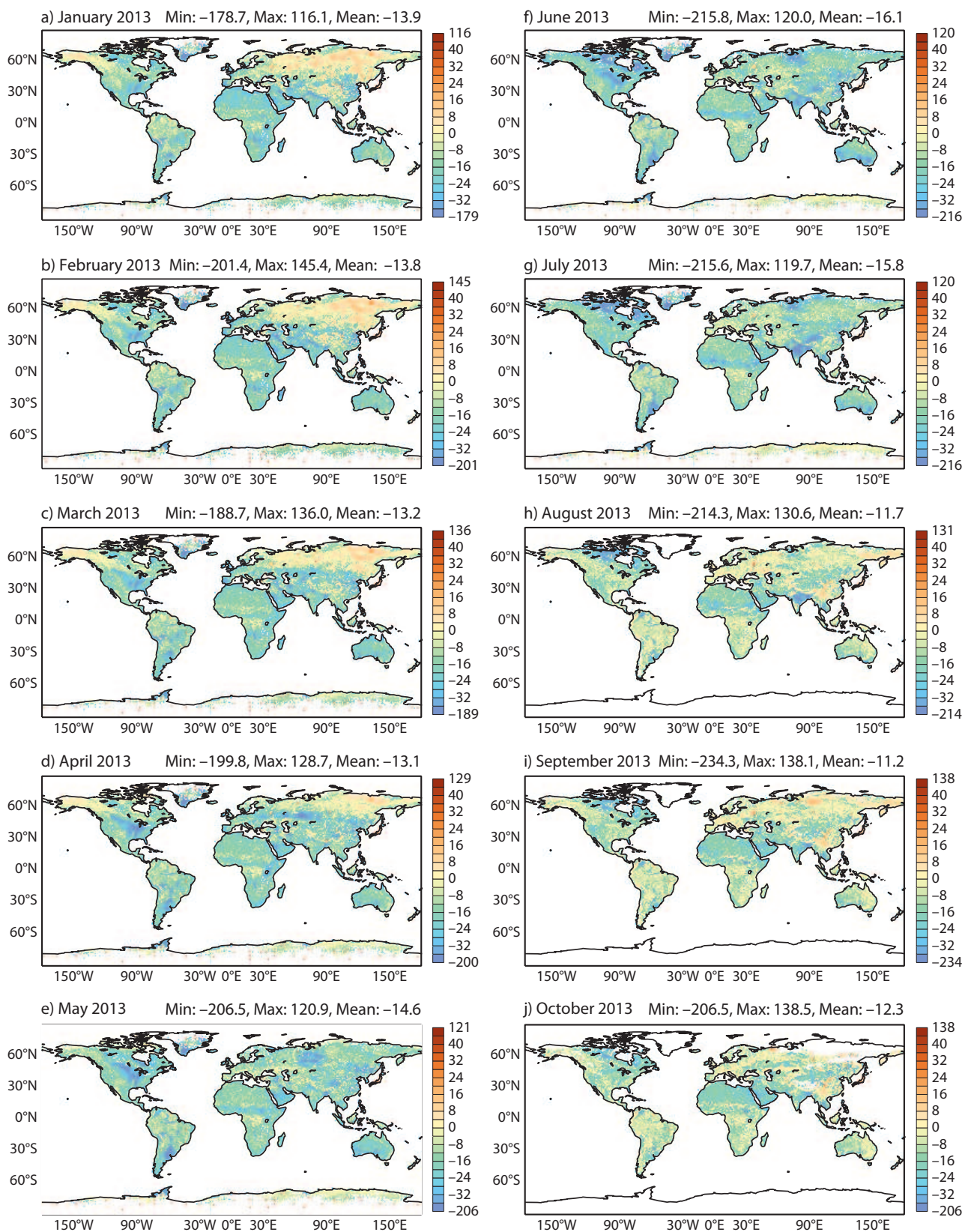


Figure 6: As in Fig. 5, but for YY polarisation.

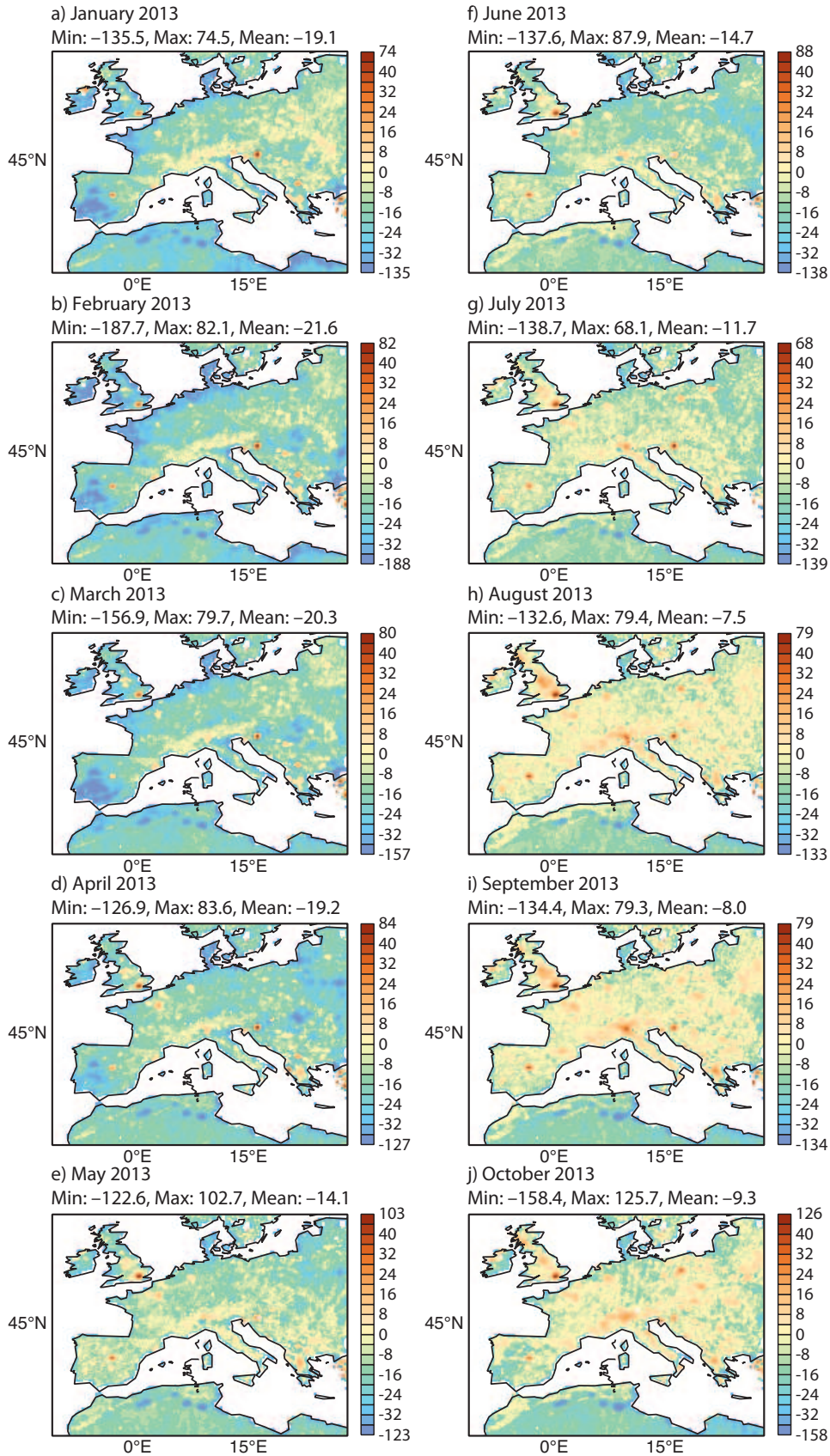


Figure 7: As in Fig. 6, but zoom in over Europe.

3.3 Time series

Figs. 8 to 15 present time series of the observed brightness temperatures, CMEM equivalents, first guess departures and number of observations, from January to December 2013. Each value represents one mean value per ECMWF 4DVAR 12 hours assimilation cycle averaged at global scale, hemisphere or continent.

Fig. 8 presents the results obtained at global scale over land pixels. Left panel is for XX polarisation and right panel for YY polarisation. This figure shows very clearly the different changes in the SMOS monitoring during 2013. In the second half of July there is a jump in the time series of bias (top panel), corresponding to the new set of CMEM parameterisations used in the operational suite (see section 3.1). The mean bias for XX polarisation decrease in average 5 K at global scale, being the reduction of the same order in YY polarisation. This decrease can not be fully associated to the absence of snow, as few grid points are covered by snow in summer of the Northern Hemisphere, but it is also due to the new roughness parameterisation which is more realistic and allows larger variability of the simulated brightness temperatures. In mid November, another jump in the time series of mean bias can also be observed. Is at this moment when the new ECMWF cycle 40r1 entered in to operations, and the CMEM platform was fully calibrated (see explanation in 3.1). This jump seems to be stronger in XX polarisation. The mean STD of bias also decrease in XX polarisation with the operational suite, however it increases slightly in YY polarisation, which is less sensitive to the influence of snow. Since the effect of snow is removed from mid July 2013, it is expected a smaller amplitude of the annual cycle of bias, especially at XX polarisation. For this polarisation, in average at global scale, the model matches quite well the observations at the end of the year. However, for YY polarisation, even with the model calibrated, the observations are still overestimated by 11 K in average at global scale. A large contribution of these negative bias can be due to the large influence of RFI in YY polarisation. For example, it is observed that the mean negative bias in the Northern Hemisphere (Fig. 9) almost doubled those of the Southern Hemisphere (Fig. 10), which is caused by RFI. However, they are not the only reason, as it can be observed in areas free of RFI as, for example, Australia (Fig. 15), where simulated brightness temperatures in YY polarisation are not accurately represented.

It is worth to observe how the number of observations is changing in 2013, in Fig. 8. Basically, three different periods can be observed; in the first one up to May, lower number of observations are counted compared to the second period, extending from May to mid July. From there, the number of observations decreases constantly until nearly the end of the year. The production of time series were very useful to detect a problem in the data downloading and which was already mentioned in (Muñoz-Sabater et al. 2013a); On 5 July 2012 the ftp repositories at ESAC were reorganized by month/day instead of by month. The last pass before midnight is since then created the day after, and the downloading script at ECMWF did not handle this change properly, which caused a systematic loss of the last orbit of the day. This problem was fixed by ECMWF shortly after detection in late April 2013. Since then it can be observed how the number of observations increases again and they are more stable. In mid July, with SMOS monitoring in the operational suite, all grid points covered by snow or affected by ice are since then rejected and not accounted for in the mean statistics. This is why the number of observations drops substantially from that date. As the coldest months approach, an increasing number of model grid points are rejected by snow or ice. In contrast, the number of observations in South America (Fig. 10) or Australia (Fig. 15) is quite stable, as being very little or not affected by snow.

The STD of the bias in the Southern Hemisphere decreases clearly with the operational suite, around 5 K, whereas the reduction is smoother in the Northern Hemisphere. In YY polarisation for this hemisphere, the level of the STD of bias is the same, but more stable due to the absence of snow. However, with the introduction of cycle 40r1 and the full calibration of CMEM, the STD of bias increases, likely due to a larger responsiveness

of the model which makes it more dynamic. Anyway, the presence of RFI in the Northern Hemisphere makes the STD of bias higher in this half of the world. As it could be expected, the largest variability of the STD of bias are found in Europe (Fig. 11) and Asia (Fig. 12), where the main RFI sources are located, with values reaching in average 35 K. In contrast, South America and Australia obtain the lowest variability of STD. In Australia, a country known to be free from RFI, there is a good range of variability of bias, around 20 K in both polarisations, which reflects the strong sensitivity to natural variations of soil moisture.

In summary, the time series shown from Fig. 8 to Fig. 15 show three different periods corresponding to different suites of SMOS monitoring and the CMEM platform calibration. The latest two months of the year, with fully calibrated CMEM platform, show a very good agreement at global scale between SMOS observed brightness temperatures and the model equivalent, whereas the observations are still overestimated in YY polarisation but at lower levels. This increases our confidence in the forward model to serve as a reliable background value for brightness temperatures in an assimilation context. Besides this, the RFI influence is still present and contaminating statistics especially in the Northern Hemisphere.

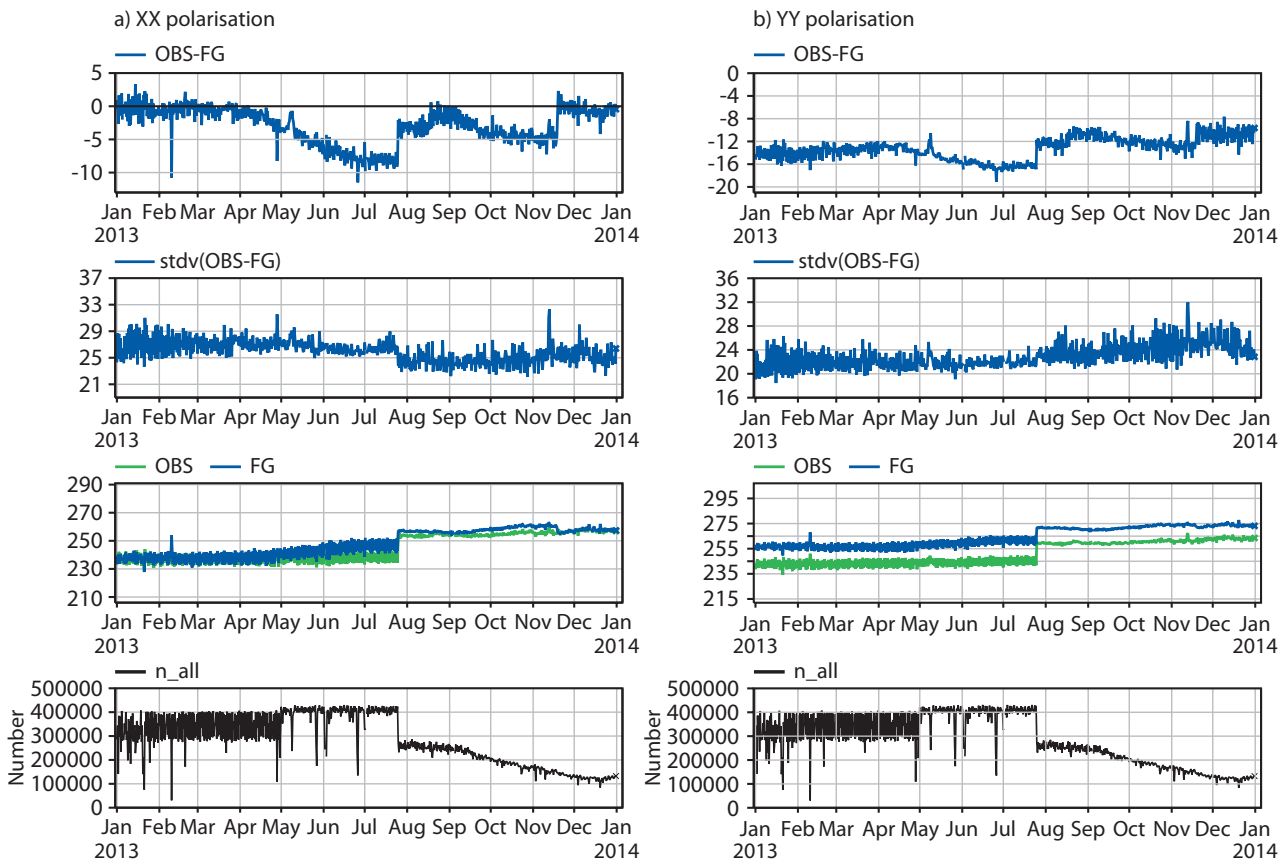


Figure 8: Global scale, time series of mean bias (top figures), mean standard deviation of bias (second top row), comparison between observed brightness temperatures and the CMEM model equivalents (third row), and number of observations (bottom figures), from January to December 2013 over continental surfaces, at 40 degrees incidence angle. Each value is an averaged value per ECMWF 4DVAR 12h cycle. Left panel is for XX polarisation, right panel for YY polarisation.

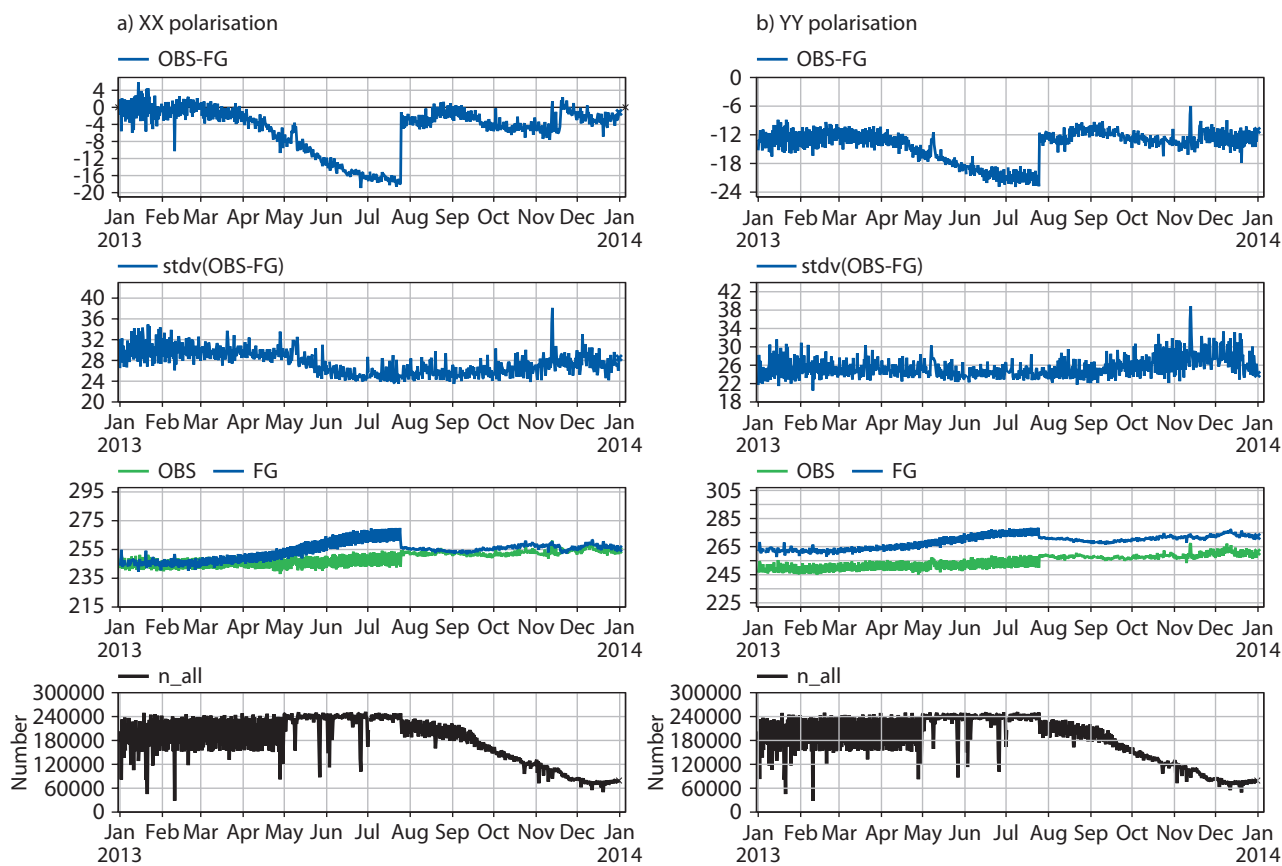


Figure 9: As in Fig. 8 but for the Northern Hemisphere.

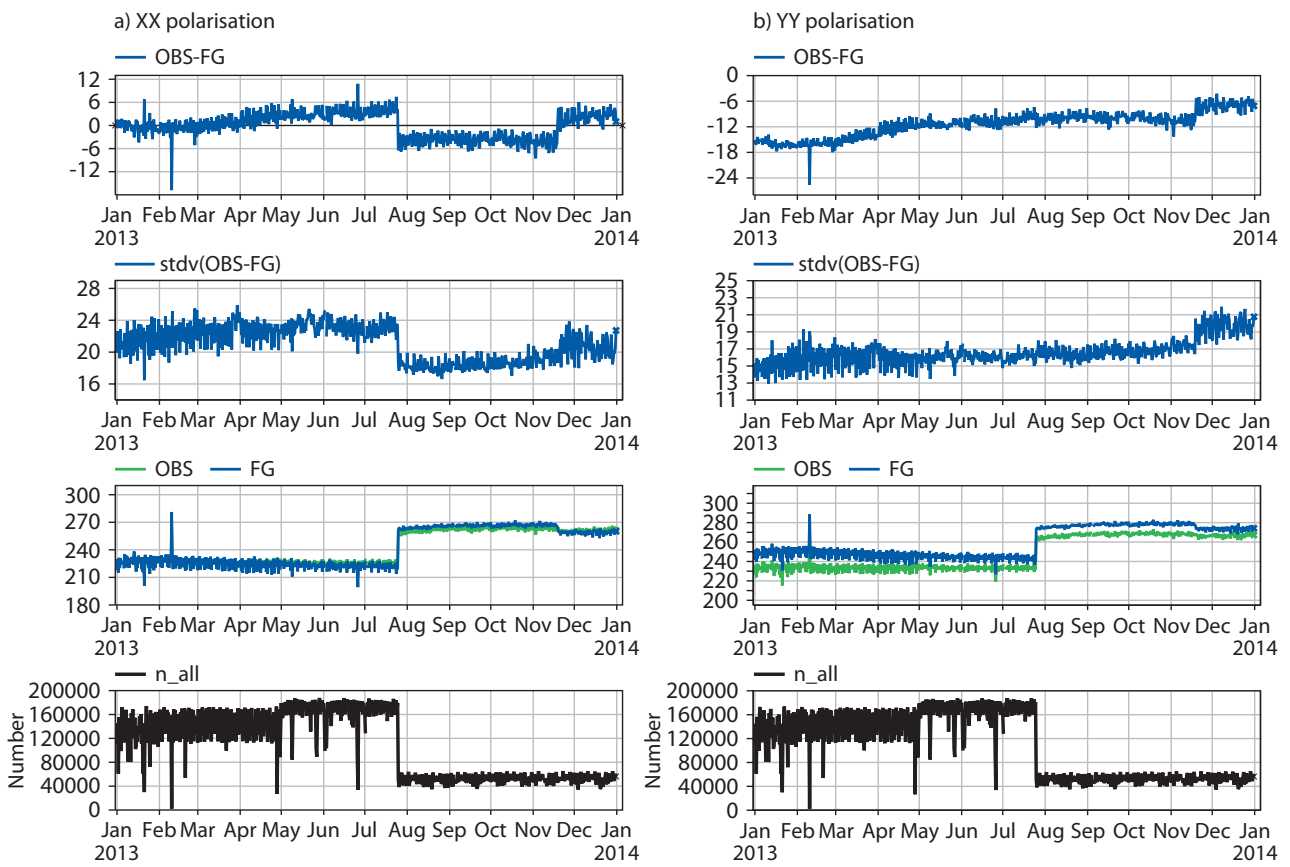


Figure 10: As in Fig. 8 but for the Southern Hemisphere.

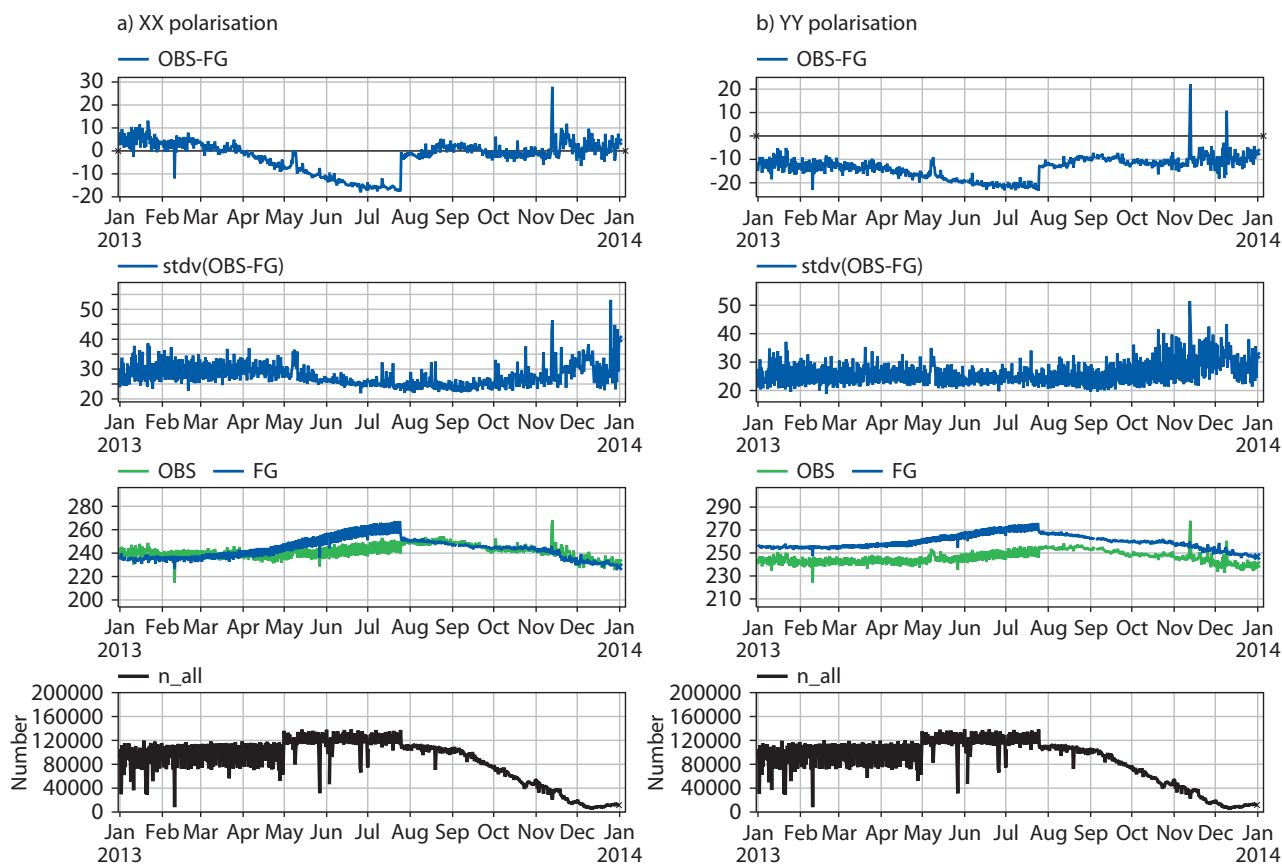


Figure 11: As in Fig. 8 but for Europe.

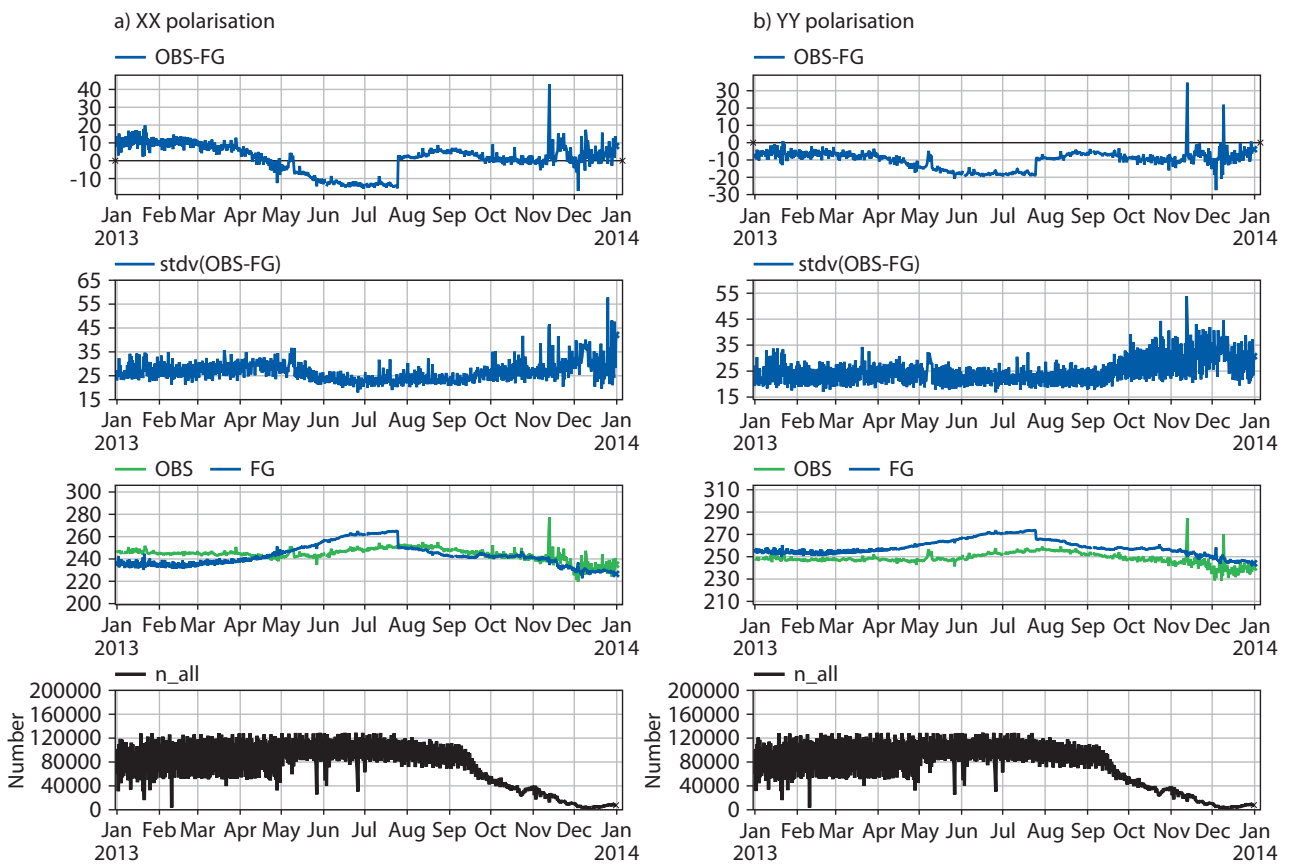


Figure 12: As in Fig. 8 but for Asia.

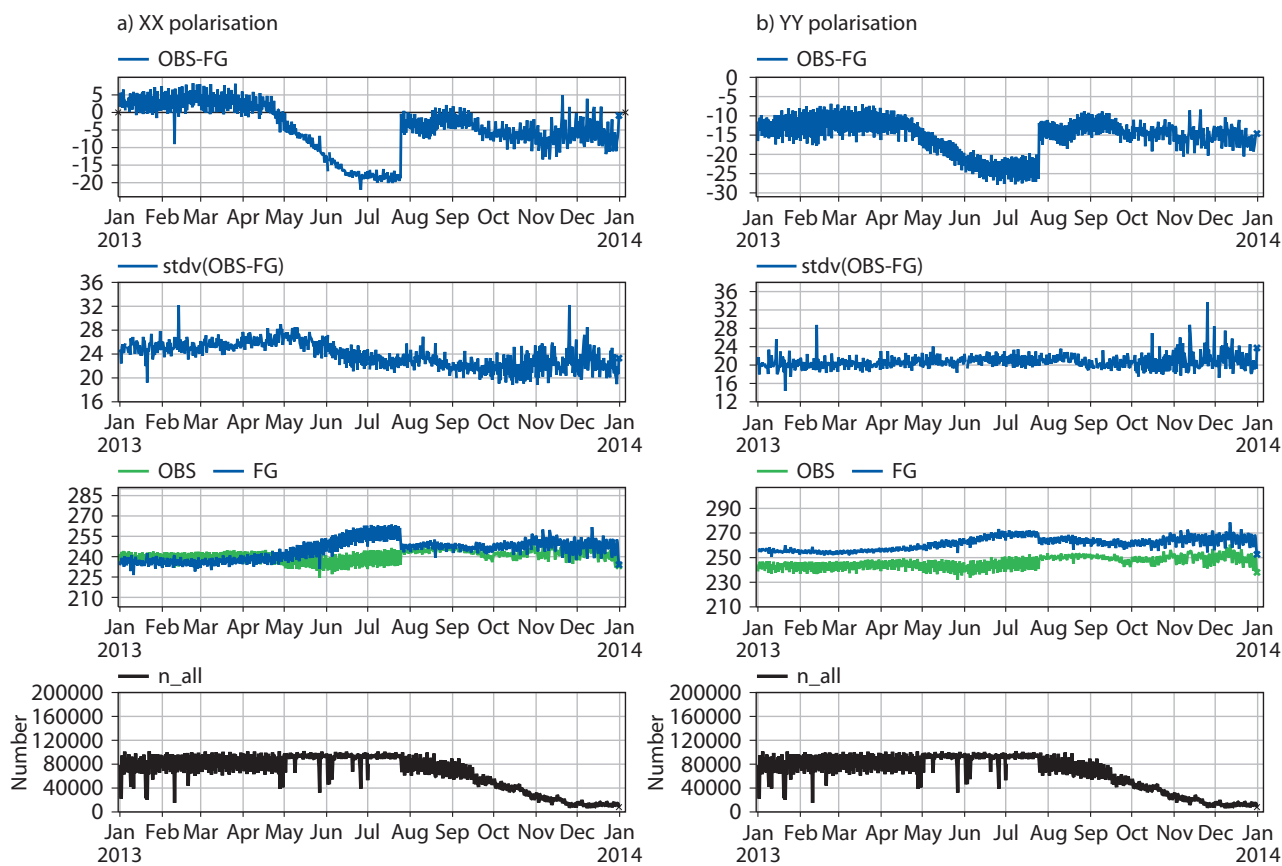


Figure 13: As in Fig. 8 but for North America.

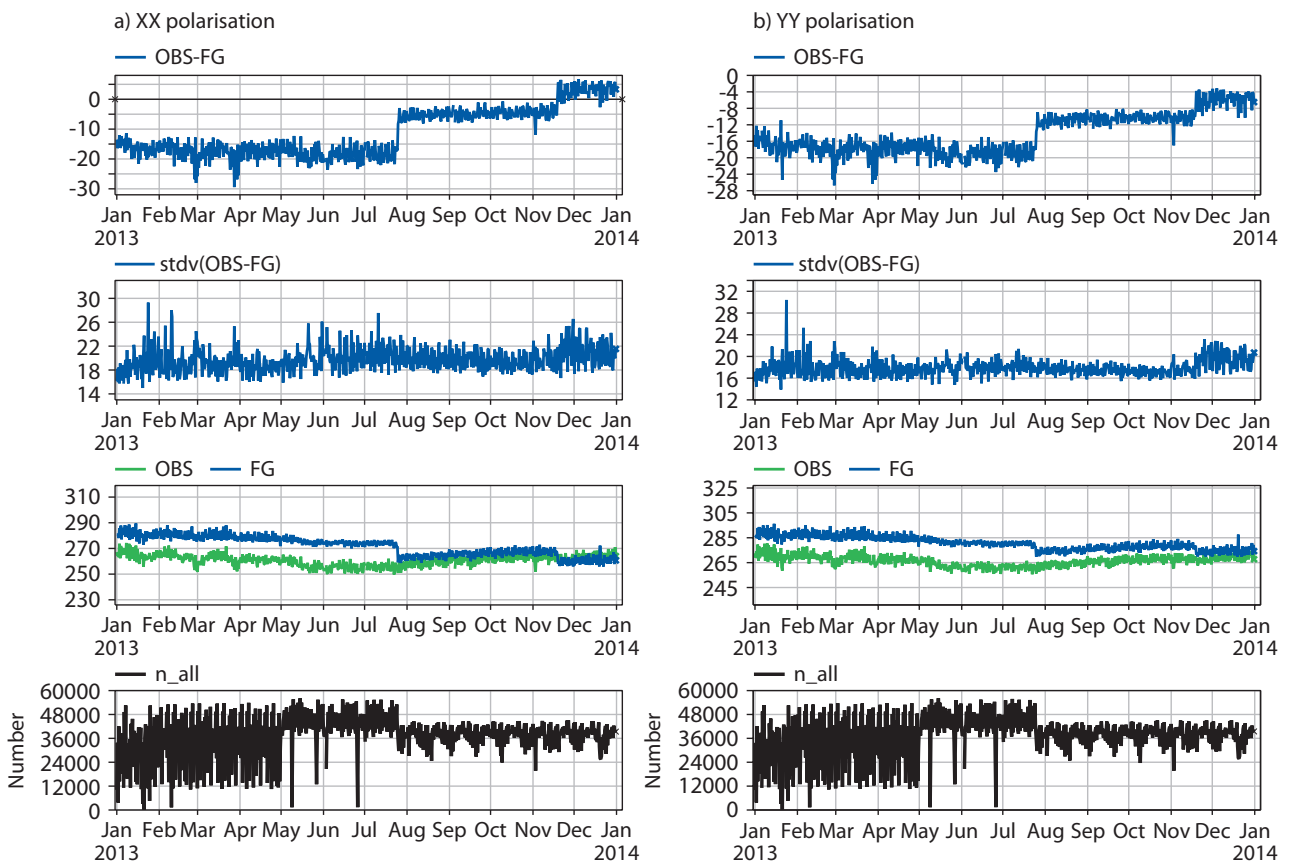


Figure 14: As in Fig. 8 but for Southern America.

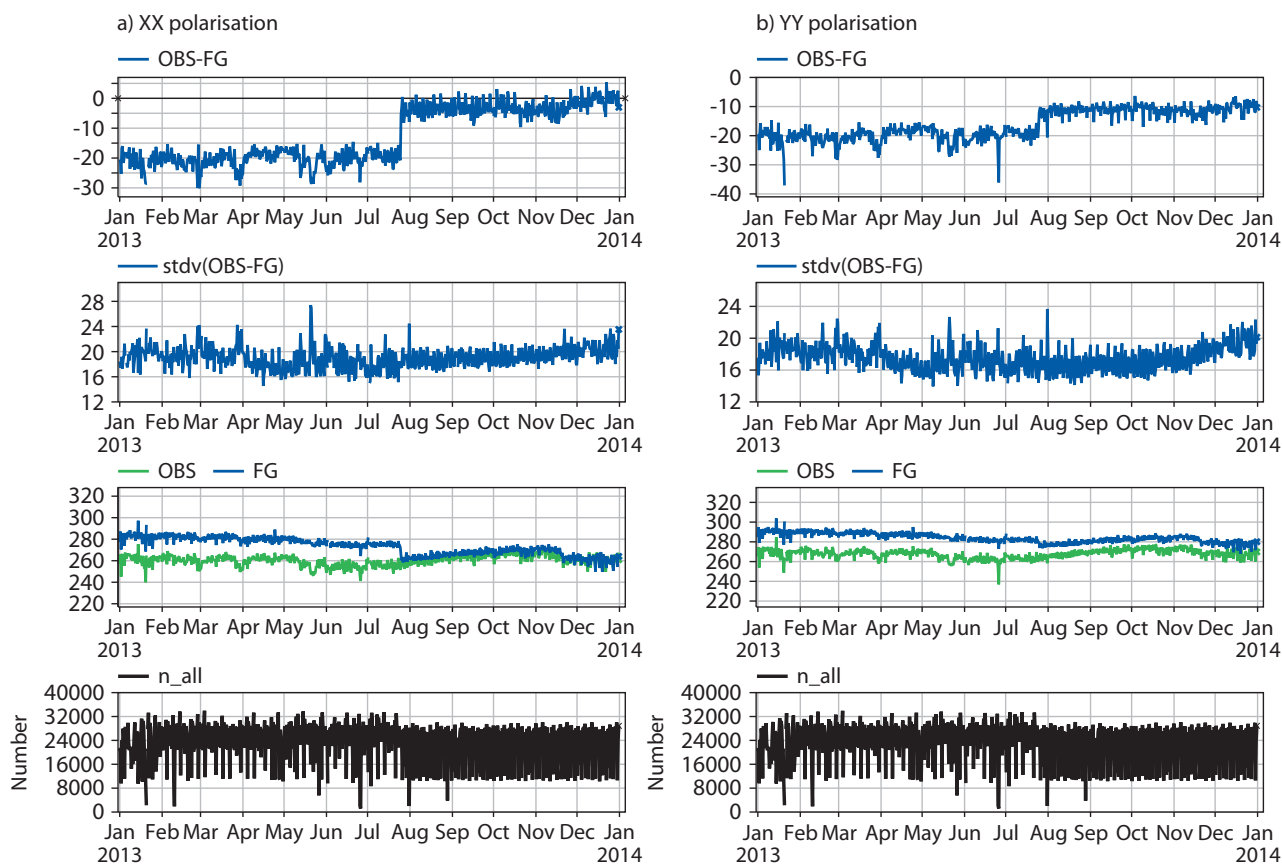


Figure 15: As in Fig. 8 but for Australia.

3.4 Angular distribution of bias

While time series presented in section 3.3 provide a good perspective of the evolution of the mean bias during the whole year, they are only valid at 40 degrees incidence angle. Bias are angular dependent too, as the viewing angle determines the spatial extent of the observed zone. In this section, the averaged results of the product showing the angular distribution of bias (named as 'scatter plots' in the website) for the period August 2013 until mid November 2013 are shown. In this way we display bias as a function of the incidence angle with one consistent set of parameterisations of the CMEM platform, and omitting the first half of the year to avoid the influence of snow in these statistics.

Fig. 16 presents the time and spatial averaged bias as a function of the incidence angle, at global scale, for the Northern and Southern Hemispheres, and separately for XX and YY polarisations. Fig. 17 presents the angular distribution of bias for some regions: Europe, North America and Australia. The coloured scale bar refers to the number of observations for each rank of bias. The total number of observations used in the assimilation system at global scale is, for this period, more than 165 millions for both polarisations, 127 millions of which belong to the Northern Hemisphere and 37 millions to the Southern Hemisphere. As expected, the number of observations is minimum for the lowest incidence angles and for all regions. For each incidence angle, the mean bias are bounded between -10 K and 0 K, which is a sign that in general the averaged bias are systematically negative and stronger for YY polarisation. A few number of observations is still remaining for very strong bias, which can be due to RFI, to the coastline effect or to grid points which were not detected and were covered by snow.

With the absence of the snow influence, the model is in very good agreement with SMOS observations, in XX polarisation, until 40 degrees incidence angle in Europe (Fig. 17a and b), North America ((Fig. 17c and d) and Australia (Fig. 17e and f). At 50 and 60 degrees, the observations are underestimated. This is different than in 2012, where for most of the incidence angles the observations were underestimated. In 2012, the mean bias for Australia at 60 degrees incidence angle and XX polarisation were larger than -40 K, whereas now are -30 K. For other angles as 20 degrees, the mean bias were close to -20 K, whereas for this period of 2013 they are close to 0 K. This demonstrates that the new roughness model accounts much better for the variability of the rough soil effect in the soil emission. This problem was already pointed out in (Muñoz-Sabater et al. 2013a). For YY polarisation the distribution of the mean bias as a function of the incidence angle is the same than in 2012. In this case, the strongest bias are found at 30 degrees, with minimum values of -15 K (a bit lower than those of 2012), and are minimum at 60 degrees, being in this case close to zero.

The year 2014 will shed new light into more realistic mean bias over longer time series, with a consistent fully calibrated version of the CMEM platform. Although they are not expected to be different to those shown in the two figures of this section, they will likely be a bit smaller in absolute values.

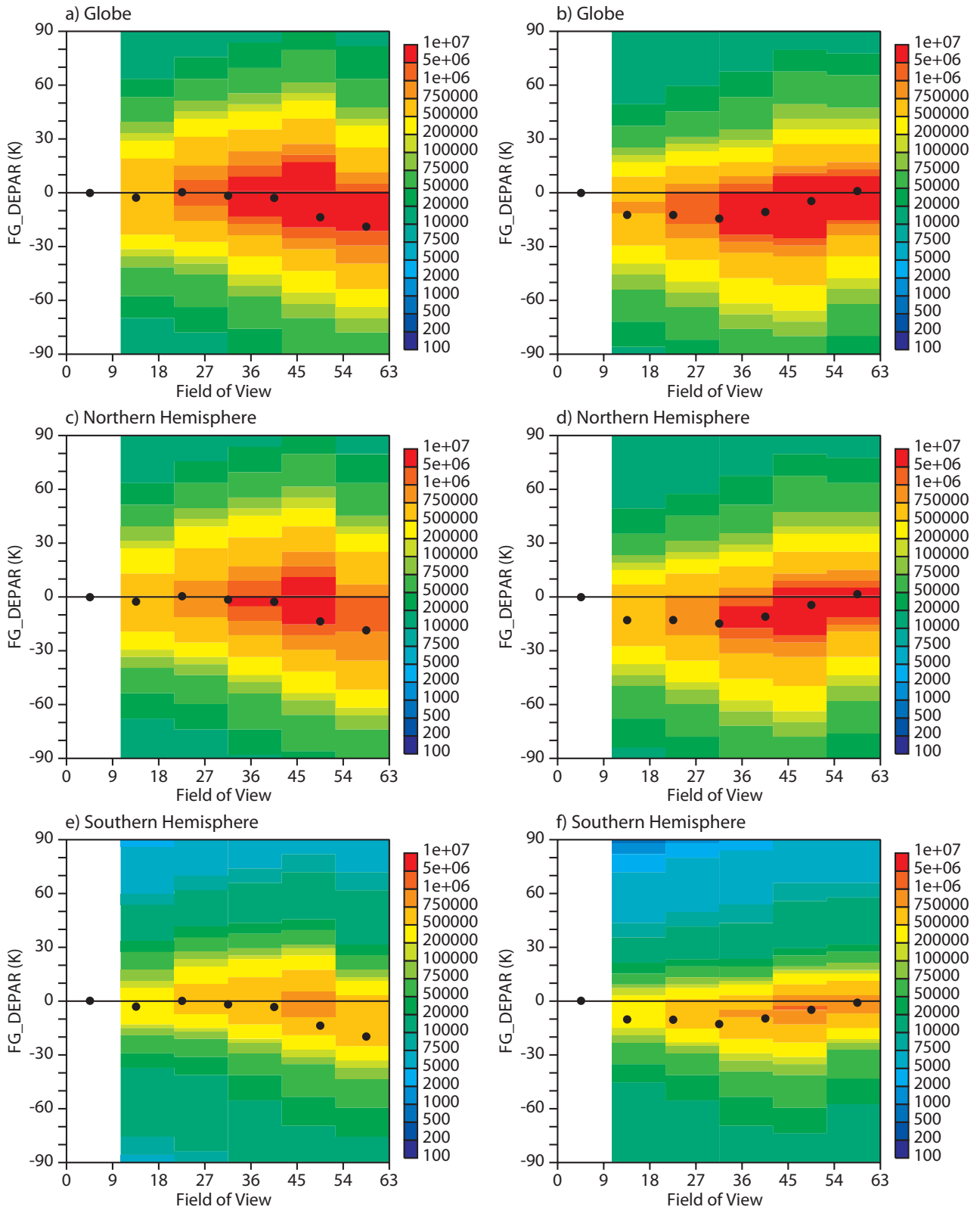


Figure 16: Mean bias as a function of the incidence angle for XX polarisation (left column) and YY polarisation (right column), for the whole year 2013. Only continental surfaces are considered in these figures.

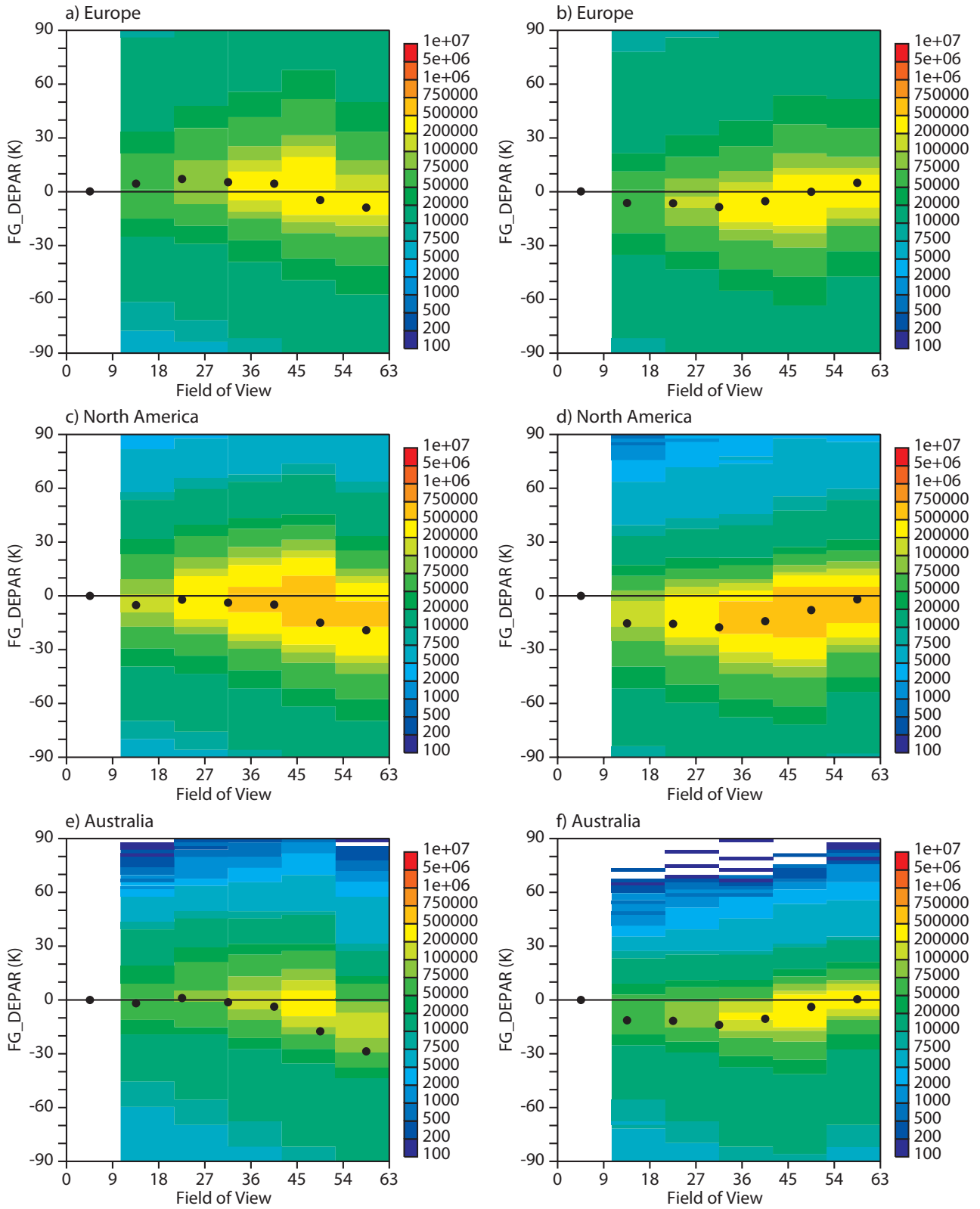


Figure 17: As Fig 16 but for Europe, North America and Australia.

3.5 Hovmöller plots

Hovmöller plots provide a latitudinal-temporal perspective of a statistical given variable. In the plots of this section, each point represents a 12h average per 2.5 degrees of latitude. They make it possible to analyse the seasonal evolution of the statistical variables under study per bands of latitude, and therefore they are very complementary of the time-averaged geographical mean fields and time series. Punctual problems in the data that could be unnoticed in time-averaged geographical plots can be easily identified in these plots.

In Fig. 18 the Hovmöller plots of the observed brightness temperatures are shown for the whole year 2013, for three incidence angles (20, 40 and 60) and XX (left column) and YY polarisation (right panel). They show the different evolution of brightness temperatures with increasing the incidence angle; they decrease for XX polarisation and increase for YY polarisation. As it was shown for the geographical plots of section 3.2, the angular range of brightness temperatures is stronger for XX polarisation in average over the whole globe and year 2013. This figure also separates clearly the moment in which SMOS monitoring became operational, as the Antarctic region and snow covered areas are not included any longer. The desert regions in both Hemispheres are clearly observed, obtaining the strongest values of brightness temperatures throughout the year. It also can be observed lower averaged brightness temperatures between May and September in latitudes around 40 degrees South, because of the winter conditions in the south of South America. These latitudes also present an apparent monthly cycle of brightness temperatures, which may be due to the few number of observations available to compute these statistics. In the next monitoring report, a whole year of latitudinal-temporal evolution of brightness temperatures with the full calibrated parameterisation of CMEM platform will be shown.

First-guess departures are presented in Fig. 19, for XX (left column) and YY polarisation (right column). The three different SMOS monitoring periods during 2013 are more evident in this figure. In the first half of the year, first-guess departures are overall dominated by snow covered areas. For this period, large departures are obtained for snow regions, as the emission over snow is strongly underestimated. However, in the second half of the year, two regions can be clearly observed in terms of bias; one with small departure values, and another one in latitudes corresponding to the desert regions of the Northern Hemisphere with slightly larger departures, where the model still clearly overestimates the soil emission. Dense vegetated latitudes show small bias, as the representation of dense vegetated canopies is quite accurate and the annual dynamic small. This is consistent with that shown in 2012. The last month and a half of the year also presents slightly different departure values, in general lower, and which reflects the new full calibration of the CMEM platform parameterisations.

Fig. 20 shows the standard deviation of the first-guess departures, for the same incidence angles and polarisations than the previous two figures. The red, non uniform band between 20 and 60 degrees North latitude reflects excessive variability of the first-guess departures and, as it occurred for previous years, is mainly due to the contamination produced by intermittent sources of RFI. Unfortunately, this effect masks the strong dynamic of brightness temperatures that was found in the US Great Plains (Muñoz-Sabater et al. 2013b). However, it still can be observed the good range of variability obtained in latitudes corresponding to Australia.

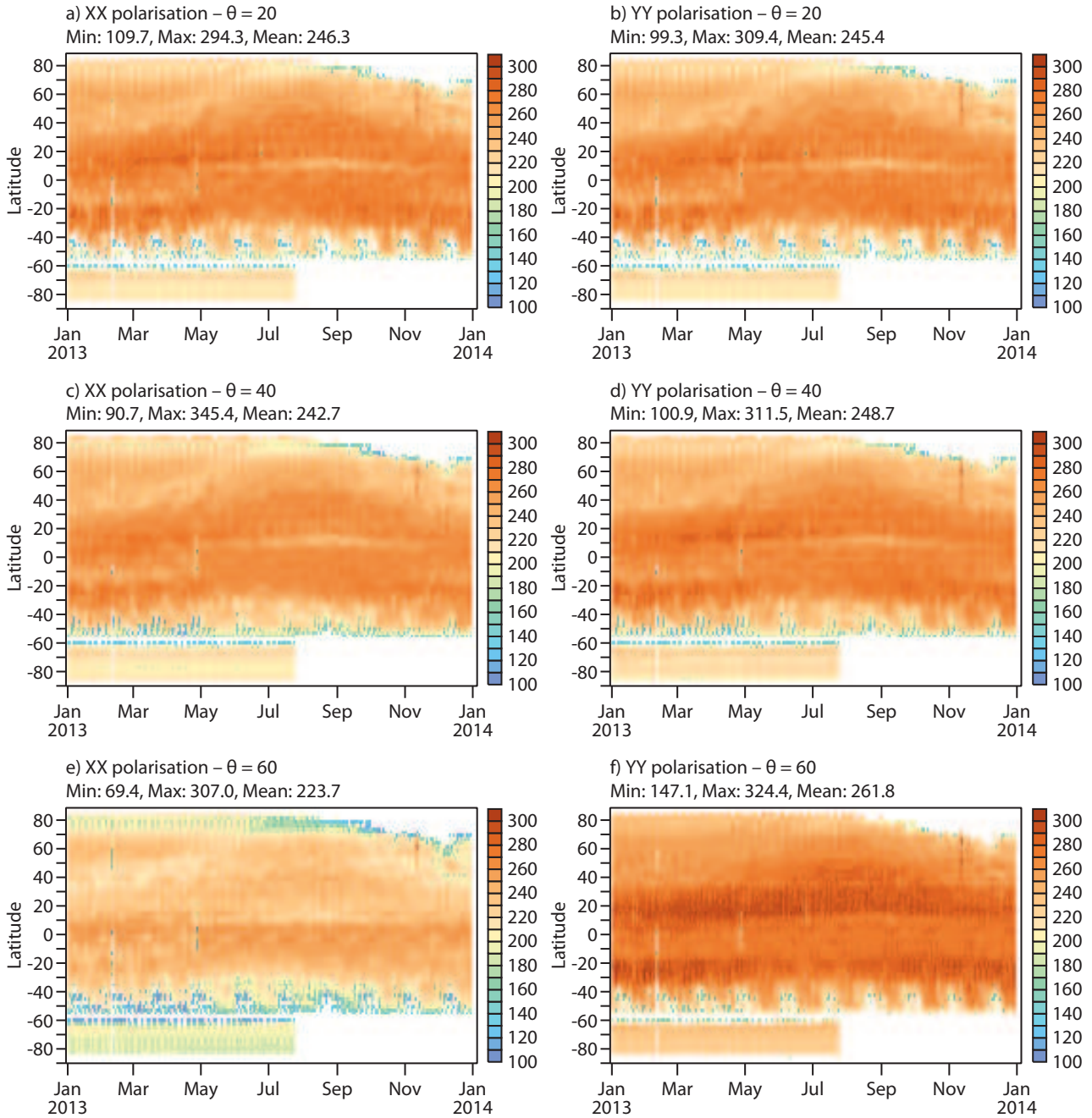


Figure 18: Mean SMOS observed brightness temperatures per bands of 2.5 degrees of latitude as a function of time. Left panel if for XX polarisation and right panel for YY polarisation. Figures are shown for 20, 40 and 60 degrees incidence angle.

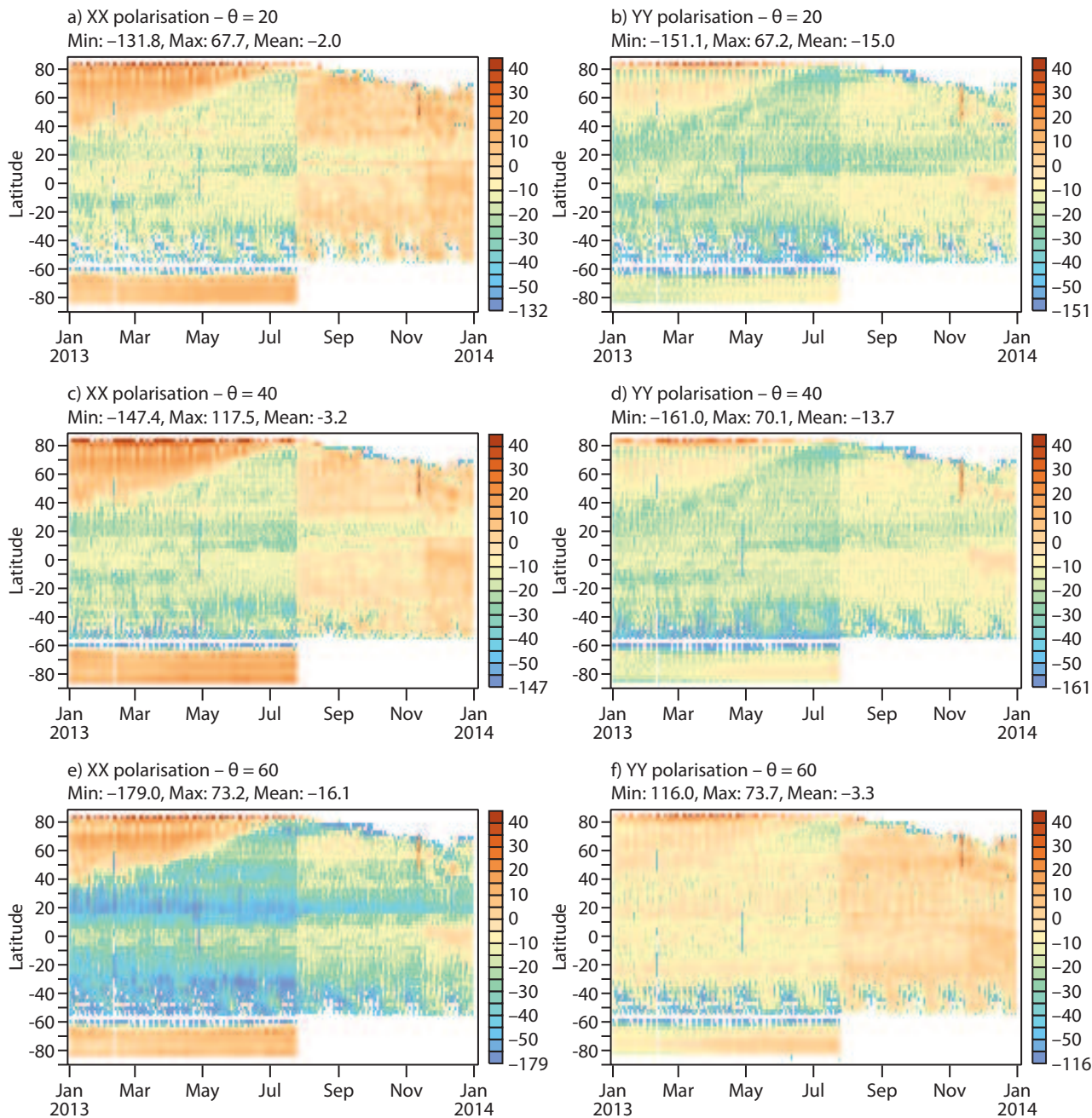


Figure 19: As in Fig. 18, but the variable shown is the first-guess departures.

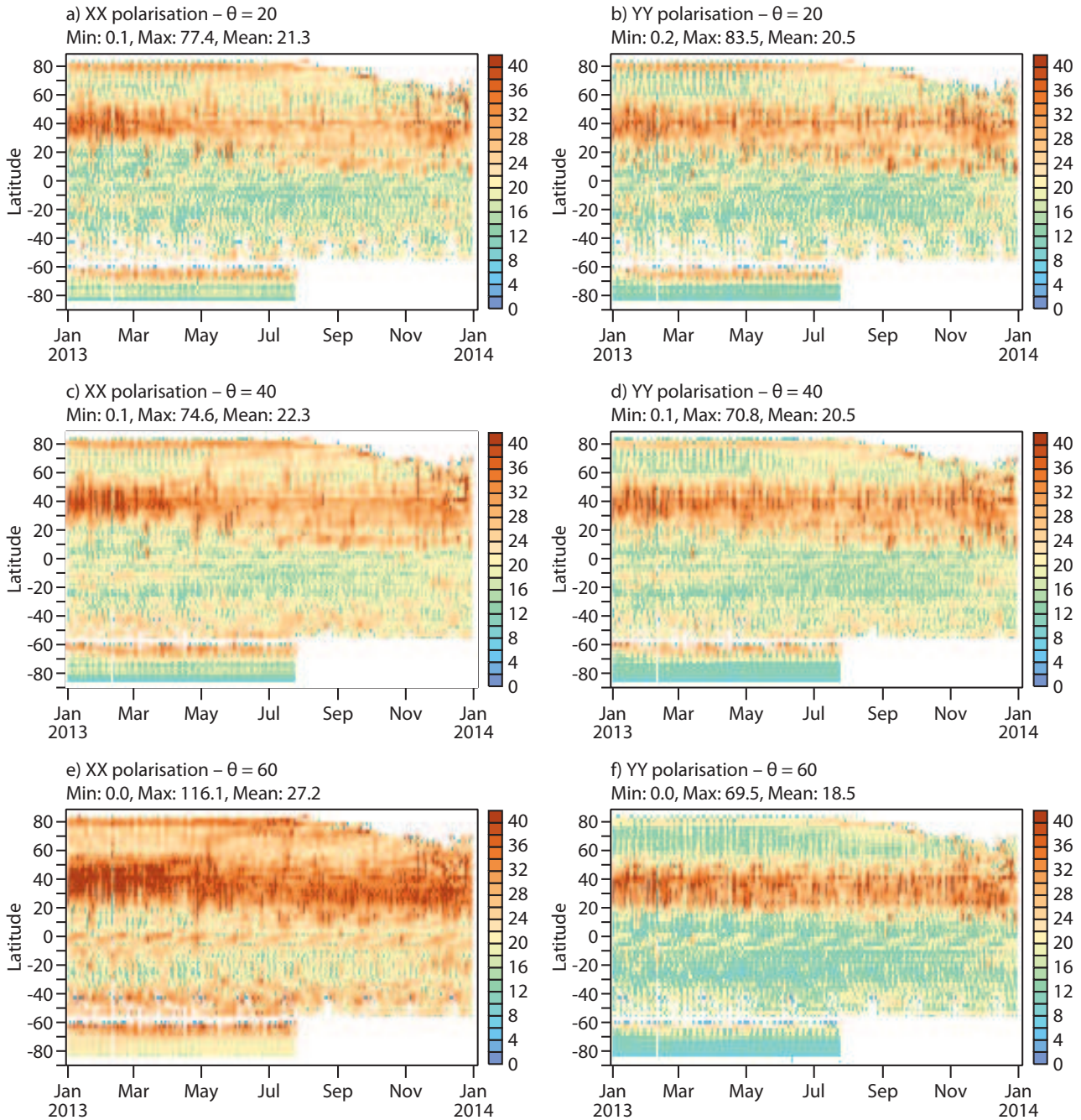


Figure 20: As in Fig. 18, but the variable shown is the first-guess departures standard deviation.

4 Monitoring over oceans

In this section some of the most relevant results obtained with the monitoring suite [see a description in part III of (Muñoz-Sabater et al. 2010) and (Muñoz-Sabater et al. 2011b)] over oceans are presented.

In (Muñoz-Sabater et al. 2011a) a substantial description of the statistical variables obtained over oceans in 2011 was given, including time-averages geographical mean fields, time series and Hovmöller plots. However, there it was pinpointed that with the current parameterisation used in CMEM, the effect of the wind and of the galactic noise in the L-band emission over oceans is not accounted for. On the contrary, it considers the ocean as a smooth surface of water. Since these two missing components are important for oceans, only statistics involving the observed brightness temperatures are presented in this report too.

4.1 Time-averaged geographical mean fields.

Fig. 21 and Fig. 22 show the averaged brightness temperatures over ocean surfaces as a function of the incidence angle for August 2013 and XX polarisation (Fig. 21) and YY polarisation (Fig. 22). Each value represents a mean value in boxes of 0.25 degrees. As it occurs over continental surfaces, brightness temperatures decrease with the incidence angle for XX polarisation and increase for YY polarisation. However the dielectric constant of water is very different of that of soil, and therefore water and soils have very different emissivity in the L-band. Significantly lower values of brightness temperatures are collected over oceans compared to land surfaces. On average 140.1 K lower for August 2013 at 50 degrees incidence angle and XX polarisation, whereas the difference is smaller at YY polarisation, 113.3 K. As expected, the angular dynamical range of brightness temperatures between 20 and 60 degrees is stronger at YY polarisation; 57.3 K compared to 26.6 K for XX polarisation. These values are consistent with those observed for previous years. The fraction of frozen open sea water in the Antarctica region can be clearly observed in these figures too, as the emissivity over a frozen surface is much larger, and therefore the observed brightness temperatures. The same effect can be observed in the Arctic region, given that in summer months still larger areas are covered by ice or snow. Brightness temperatures over oceans have a much lower dynamical range compared to land surfaces, as they are relatively more homogeneous.

The evolution of the SMOS observed brightness temperatures standard deviation in the XX polarisation at 40 degrees incidence angle, from January to October 2013 (one averaged value per month), is shown in Fig. 23. Fig. 24 is the equivalent figure for YY polarisation. The spatial resolution is 0.25 degrees. These values are very much in line with those of years 2011 and 2012. Also the situation of RFI contamination in open waters in 2013 is the same than for previous years near the coastlines of China, Middle East and Eastern European. The contamination is not only limited to coastlines, but in some cases several hundred of kilometers offshore. The plots for September and October 2013 show also statistics over land masses. These areas of land correspond to regions where snow was detected and a water flag was assigned. A new snow flag has already been introduced in operations, and this effect will not be present in the plots corresponding to 2014.

As it was also reported in (Muñoz-Sabater et al. 2011a) and (Muñoz-Sabater et al. 2013a), the transition zone between frozen and liquid water over Antarctica is clearly observed in Figs. 23 and Fig. 24. The reason is the very different dielectric properties of frozen and liquid water, and therefore presenting very different emissivities. As this is a very sensitive and dynamical zone, the variability of brightness temperatures is very large. During the summer months at the Southern Hemisphere this transition zone can barely be observed, or at least is very close to the Antarctica continent, whereas it moves far from the coastline during the winter months.

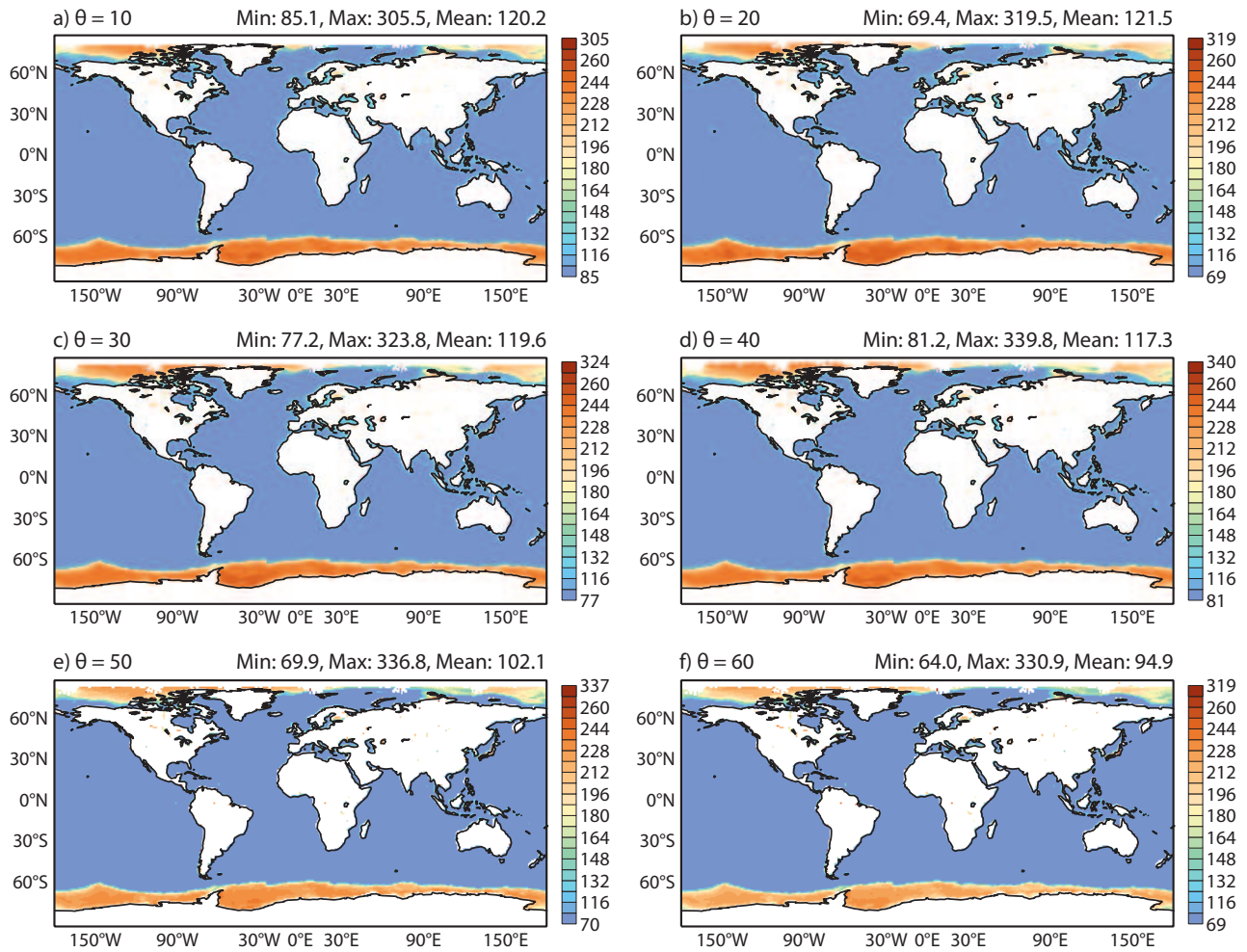


Figure 21: August 2013, angular global mean of the SMOS observed brightness temperatures for ocean surfaces and for XX polarisation. Each value represents a mean value of all the data inside a box of 0.25 degrees.

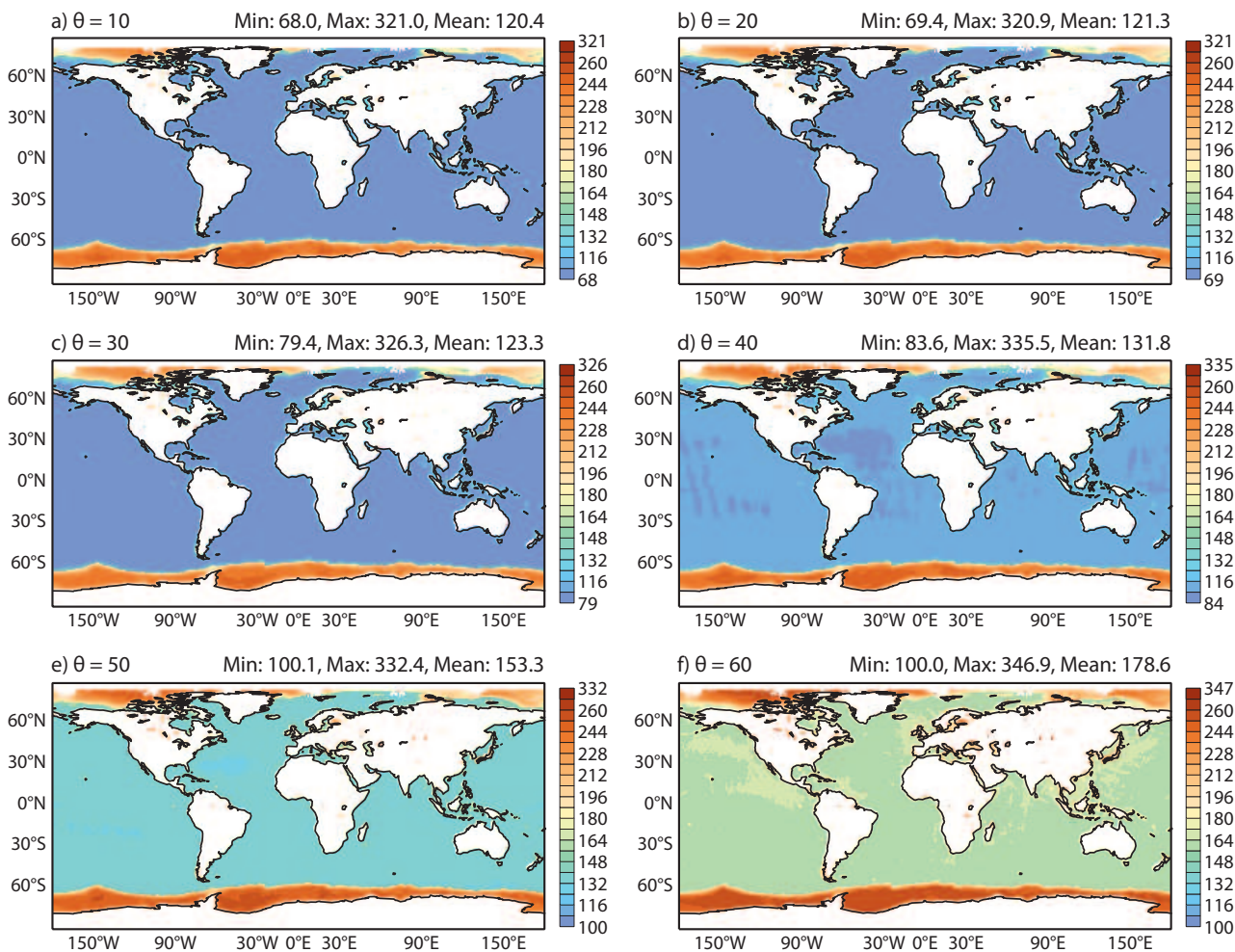


Figure 22: As in Fig. 21 but for YY polarisation.

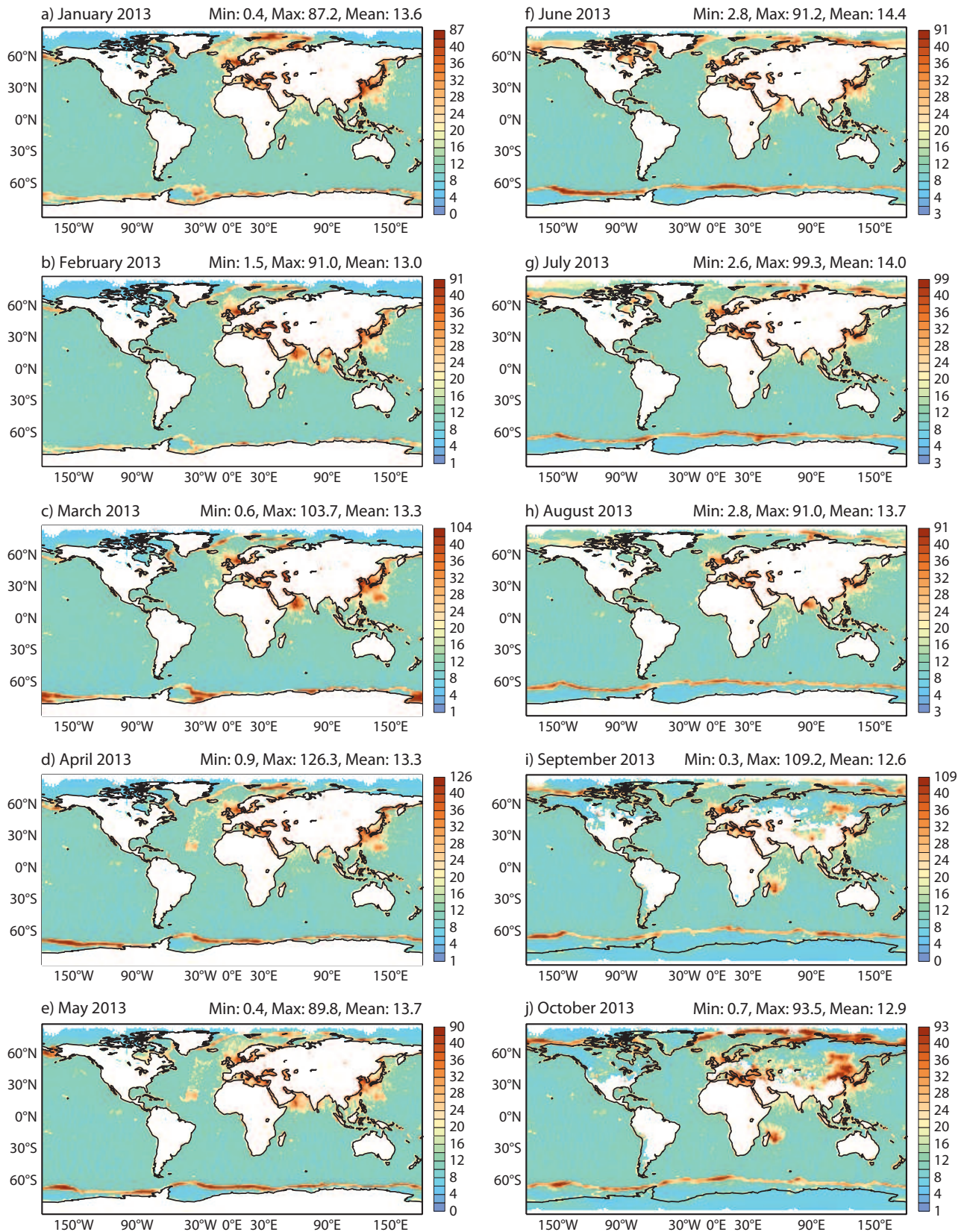


Figure 23: Monthly mean of the SMOS observed brightness temperatures standard deviation, for XX polarisation and for ocean surfaces only. Each value represents a mean value of all the data inside a box of 0.25 degrees. The incidence angle is 40 degrees.

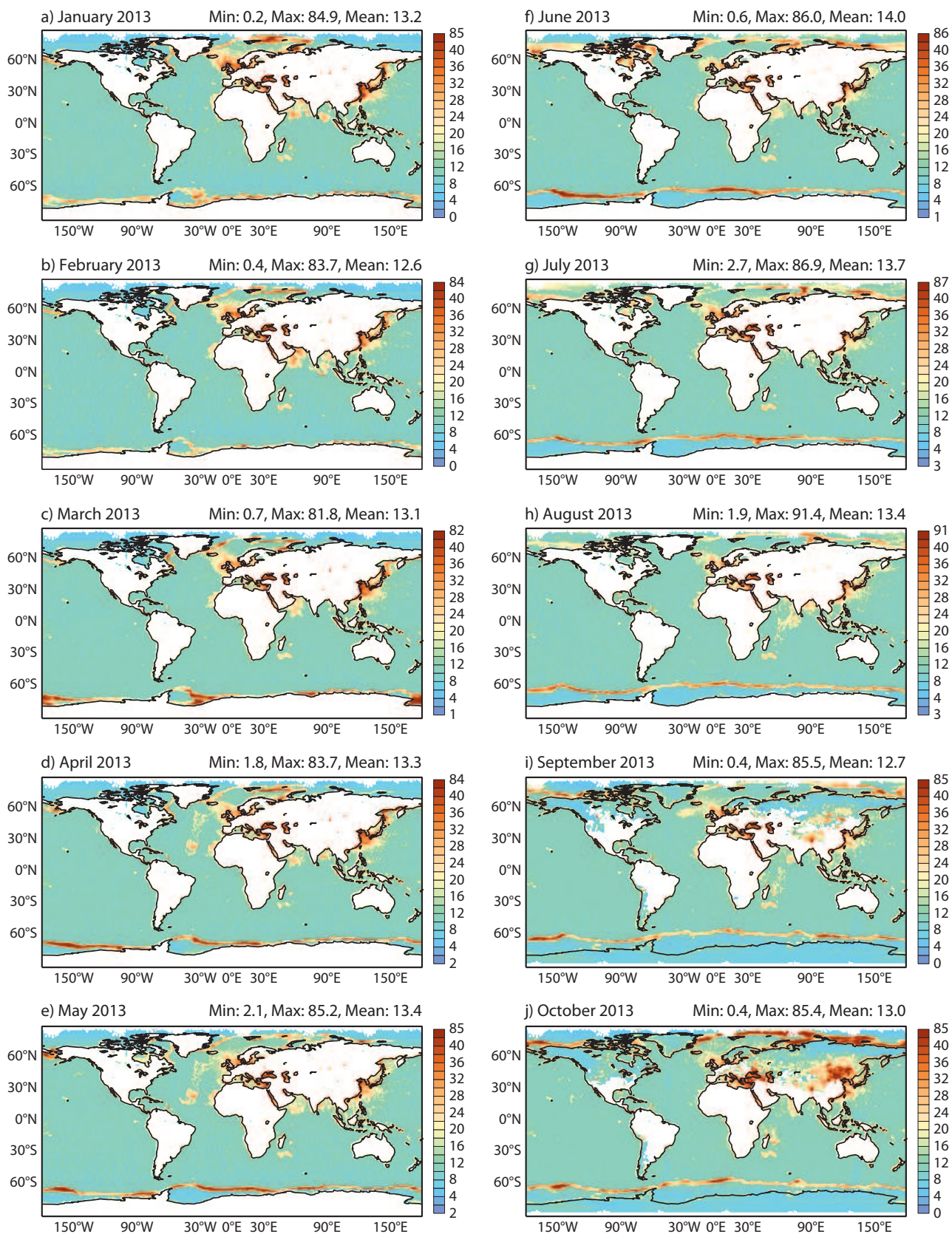


Figure 24: As Fig. 23 but for YY polarisation.

4.2 Hovmöller plots

Fig. 25 shows the latitudinal-temporal evolution of the observed brightness temperatures, averaged per bands of 2.5 degrees of latitude from January to October 2013. They are produced at 20, 40 and 60 degrees incidence angle and for XX and YY polarisations. The evolution of the fraction of frozen sea around the poles can be clearly seen in this figure, as they present contrasting larger brightness temperatures than the rest of the seas. They are maximum between June and November 2013 at the Southern Hemisphere, coinciding with the minimum of the Northern Hemisphere. On the contrary that over land masses, all water phases in the oceans (liquid or frozen) are monitored, as brightness temperatures at ECMWF are not assimilated over the oceans. As it should be, brightness temperatures clearly decrease with increasing the incidence angle for XX polarisation, while comparatively they increase much faster for YY polarisation.

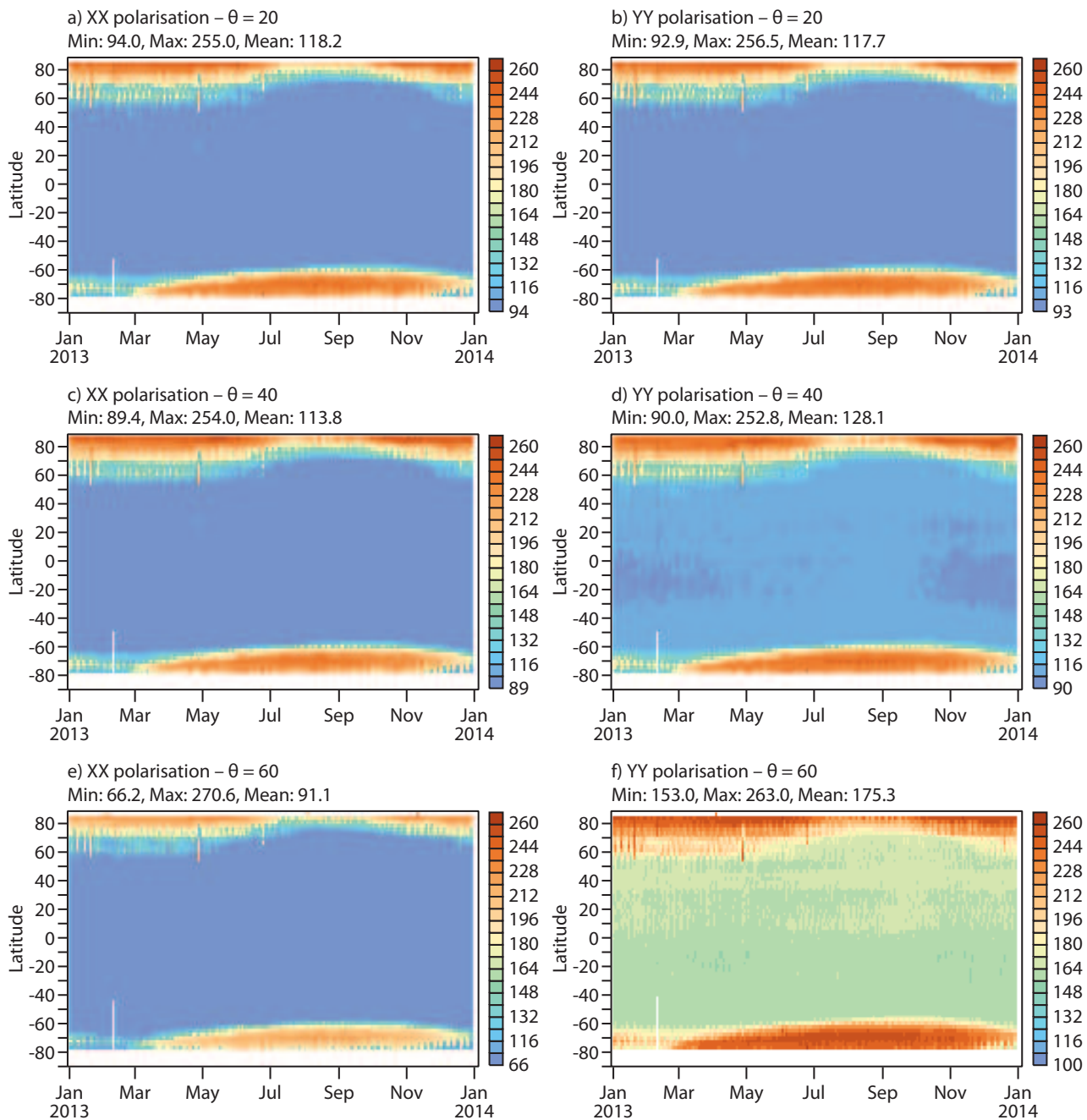


Figure 25: Mean SMOS observed brightness temperatures per bands of 2.5 degrees of latitude as a function of time, only over oceans. Left panel if for XX polarisation and right panel for YY polarisation. Figures are shown for 20, 40 and 60 degrees incidence angle.

5 Summary

This is the fourth report on SMOS observed brightness temperatures, model equivalents and first-guess departures for the whole year 2013. It presents NRT statistics corresponding to three ECMWF cycles; cycle 37r3 under which the SMOS monitoring suite was running, as for the year 2012, cycle 38r2, where SMOS monitoring entered into operations, and cy40r1 which is operational since 19 November 2013. The ECMWF passive microwaves emission CMEM platform is used to simulate brightness temperatures at the top of the atmosphere. Geolocated SMOS observed brightness temperatures in the Icosahedron Snyder Equal Area (ISEA) at aperture 4 and resolution 9 grid are compared to CMEM estimations geolocated at the ECMWF spectral horizontal truncation T511 (approximately 40 km), at the satellite antenna reference frame and in NRT. A whole annual cycle of statistical variables was computed and analysed.

Observed brightness temperatures during the whole year 2013 behaved as expected, both for land and oceans. This means, they decrease with the incidence angle for XX polarisation and they increase for YY polarisation. However, the dynamical amplitude of brightness temperature with the incidence angle is greater for XX polarisation over lands, indicating a larger sensitivity to soil water variations. The contrary is observed over oceans, where the rate of increase with the incidence angle, in YY polarisation, is much higher than the rate of decrease for XX polarisation. For oceans, this document only reports on observed brightness temperatures, as the simulation of the microwave ocean emission does not account for the galactic noise and wind components, being the latter one a crucial component in accurate estimation of brightness temperatures over oceans.

From mid July 2013 SMOS monitoring is part of the operational suite. Two important changes were introduced. Firstly, grid points affected by snow or ice are since then rejected, as they will not be accounted for in assimilation experiments. In this context, the number of observations monitored in the Northern Hemisphere are much lower compared to previous reports. Secondly, the key parameterisations of the CMEM platform were reviewed by comparing SMOS reprocessed NRT observations with averaged simulated values of brightness temperatures with different combinations of parameterisations. The new parameterisation introduced in the operational suite demonstrated a more realistic simulation of the soil microwave emission, and in particular the new representation of rough soils allowed a larger more realistic variability of the soil emissivity. In general, this change introduced a decrease in the mean bias of 5 K at global scale, with larger differences depending on the region under analysis. The analysis of the mean bias as a function of the incidence angle also showed a more realistic simulation of brightness temperatures, with mean bias close to zero for the lowest incidence angles in XX polarisation and for the largest angles for YY polarisation. However, there are still inaccuracies to simulate the largest incidence angles in XX polarisation and middle angles in YY polarisation. In both cases, the model overestimates the observations.

Recently, with cycle 40r1, the full calibrated CMEM platform was introduced in operations. It included changes in the soil dielectric parameterisation and vegetation opacity model. The improvements in the results are more modest than those introduced in mid July, however they go in the right direction, as mean bias decreased further. In this report, only a month a half of results using the the new set of parameterisation are shown. This calibration is hereafter frozen and time series in 2014 will allow to analyse a full year of simulated values.

Although this report has shown that the current situation of RFI is much better compared to previous years, it still points to the strong influence in many of the statistics, especially visible in the variability of the observations in the Northern Hemisphere. Special care has to be put into filtering the most contaminated data when running assimilation experiments, as their influence in soil moisture increments can be very detrimental for accurate

estimates of soil moisture analysis and the influence in the forecast skill.

Acknowledgements

This work is funded under the ESA-ESRIN contract number 4000101703/10/NL/FF/fk and is the fourth (MR4) of a series of Monitoring Reports to ESA. The authors would like to thank Ioannis Mallas at ECMWF, for the operational acquisition and contribution to the processing of the data. Also many thanks to the graphic team at ECMWF for their help with the figures shown in this report.

6 References

References

- [Balsamo et al. 2009] Balsamo, G., P. Viterbo, A. Beljaars, B. van den Hurk, M. Hirschi, A. Betts, and K. Scipal, 2009 : A revised hydrology for the ECMWF model: Verification from field site to terrestrial water storage and impact in the integrated forecast system. *Journal of Hydrometeorology*, **10**,623–643. doi: 10.1175/2008JHM1068.1.
- [Choudhury et al. 1979] Choudhury, B. J., T. J. Schmugge, A. Chang, and R. W. Newton, 1979 : Effect of surface roughness on the microwave emission for soils. *Journal of Geophysical Research*, **84**,5699–5706.
- [de Rosnay et al. 2009a] de Rosnay, P., M. Drusch, A. Boone, G. Balsamo, B. Decharme, P. Harris, Y. Kerr, T. Pellarin, J. Polcher, and J.-P. Wigneron, 2009a : AMMA Land Surface Model Intercomparison Experiment coupled to the Community Microwave Emission Model: ALMIP-MEM. *J. Geophys. Res.*, **114**. D05108, doi:10.1029/2008JD010724.
- [de Rosnay et al. 2009b] de Rosnay, P., M. Drusch, and J. Muñoz-Sabater, 2009b : Milestone 1 Technical Note Part I: SMOS global surface emission model. Technical report, European Centre for Medium-Range Weather Forecast, Reading, United Kingdom.
- [de Rosnay et al. 2014] de Rosnay et al., P., 2014 : SMOS Report on bias correction. Technical report, European Centre for Medium-Range Weather Forecasts, Reading, United Kingdom.
- [Drusch et al. 2009] Drusch, M., T. Holmes, P. de Rosnay, and G. Balsamo, 2009 : Comparing ERA-40 based L-band brightness temperatures with Skylab observations: A calibration / validation study using the Community Microwave Emission Model. *J. Hydrometeor.*, **10**,213–226. doi: 10.1175/2008JHM964.1.
- [Drusch et al. 2001] Drusch, M., E. Wood, and T. Jackson, 2001 : Vegetative and atmospheric corrections for the soil moisture retrieval from passive microwave remote sensing data: Results from the southern great plains hydrology experiment 1997. *J. Hydrometeor.*, **2**,181–192.
- [Holmes et al. 2008] Holmes, T., M. Drusch, J.-P. Wigneron, and R. de Jeu, 2008 : A global simulation of microwave emission: Error structures based on output from ECMWFs operational integrated forecast system. *IEEE Transactions on Geoscience and Remote Sensing*, **46**,846 – 856.
- [Jackson and Schmugge 1991] Jackson, T. J., and T. Schmugge, 1991 : Vegetation effects on the microwave emission of soils. *Remote Sens. of Environ.*, **36**,203–212.
- [Kirdyashev et al. 1979] Kirdyashev, K., A. Chukhlantsev, and A. Shutko, 1979 : Microwave radiation of the earth's surface in the presence of vegetation cover. *Radiotekhnika i Elektronika*, **24**,256–264.
- [Matos and Gutierrez 2004] Matos, P., and A. Gutierrez, 2004 : SMOS L1 processor discrete global grids document. Technical report, Deimos Engenharia, Lisboa, Portugal.
- [Mironov et al. 2004] Mironov, V., M. Dobson, V. Kaupp, S. Komarov, and V. Kleshchenko, 2004 : Generalized refractive mixing dielectric model for moist soil. *IEEE Trans. Geosc. Remote Sens.*, **42**,773–785.
- [Muñoz-Sabater et al. 2011a] Muñoz-Sabater, J., M. Dahoui, P. de Rosnay, and L. Isaksen, 2011a : SMOS Monitoring Report; Part II. Technical report, European Centre for Medium-Range Weather Forecasts, Reading, United Kingdom.

- [Muñoz-Sabater et al. 2013a] Muñoz-Sabater, J., M. Dahoui, P. de Rosnay, and L. Isaksen, 2013a : SMOS Monitoring Report; Number III: Dec. 2011 - Dec. 2012. Technical report, European Centre for Medium-Range Weather Forecasts, Reading, United Kingdom.
- [Muñoz-Sabater et al. 2011b] Muñoz-Sabater, J., P. de Rosnay, and M. Dahoui, 2011b : SMOS Continuous Monitoring Reports; Part I. Technical report, European Centre for Medium-Range Weather Forecasts, Reading, United Kingdom.
- [Muñoz-Sabater et al. 2010] Muñoz-Sabater, J., P. de Rosnay, and A. Fouilloux, 2010 : Milestone 2 Technical Note, Part I:operational pre-processing chain, Part II:collocation software development, Part III: Offline monitoring suite. Technical report, European Centre for Medium-Range Weather Forecasts, Reading, United Kingdom.
- [Muñoz-Sabater et al. 2011c] Muñoz-Sabater, J., P. de Rosnay, and G.Balsamo, 2011c : Sensitivity of L-band NWP forward modelling to soil roughness. *Int. J. Remote Sens.*, **32**,5607–5620. iFirst 2011., doi: 10.1080/01431161.2010.507260.
- [Muñoz-Sabater et al. 2013b] Muñoz-Sabater, J., P. de Rosnay, and L. Isaksen, 2013b : SMOS report on hot-spots. Technical report, European Centre for Medium-Range Weather Forecasts, Reading, United Kingdom.
- [Pellarin et al. 2003] Pellarin, T., J.-P. Wigneron, J.-C. Calvet, and P. Waldteufel, 2003 : Global soil moisture retrieval from a synthetic l-band brightness temperature data set. *Journal of Geophysical Research*, **108**.
- [Salgado 1999] Salgado, R., 1999 : Global soil maps of sand and clay fractions and of the soil depth for MESONH simulation based on FAO/UNESCO soil maps. Technical report, CNRM/Météo France. Tech. Note, **59**.
- [Wang and Schmugge 1980] Wang, J. R., and T. Schmugge, 1980 : An empirical model for the complex dielectric permittivity of soils as a function of water content. *IEEE Transactions on Geoscience and Remote Sensing*, **18**,288–295.
- [Wigneron et al. 2007] Wigneron, J.-P., Y. Kerr, P. Waldteufel, K. Saleh, M.-J. Escorihuela, P. Richaume, P. Ferrazzoli, P. de Rosnay, R. Gurney, J.-C. Calvet, J. Grant, M. Guglielmetti, B. Hornbuckle, C. Mtzler, T. Pellarin, and M. Schwank, 2007 : L-band microwave emission of the biosphere (L-MEB) model: Description and calibration against experimental data sets over crop fields. *Remote Sensing of Environment*, **107**,639–655.
- [Wigneron et al. 2001] Wigneron, J. P., L. Laguerre, and Y. Kerr, 2001 : A simple parameterization of the L-band microwave emission from rough agricultural soils. *IEEE Transactions on Geoscience and Remote Sensing*, **39**,1697–1707.